Materials & Design 269 (2026) 116665

Contents lists available at ScienceDirect

Materials & Design

journal homepage: www.elsevier.com/locate/matdes

Investigations on the microstructural degradation and mechanical response of Ni–CGO anodes using phase-field method and stochastic modeling

Ahmed Elmoghazy [a,*], Sabrina Weber [b], Ravi Kumar Jeela [c], Andreas Prahs [a,d], Benedikt Prifling [b], Daniel Schneider [a,c,d], Volker Schmidt [b], Britta Nestler [a,c,d]

[a] Institute for Applied Materials - Microstructure Modelling and Simulation (IAM-MMS), Karlsruhe Institute of Technology (KIT), Straße am Forum 7, Karlsruhe, 76131, Germany
[b] Institute of Stochastics, Ulm University, Helmholtzstraße 18, Ulm, 89069, Germany
[c] Institute of Digital Materials Science (IDM), Karlsruhe University of Applied Sciences, Moltkestraße 30, Karlsruhe, 76133, Germany
[d] Institute of Nanotechnology (INT), Karlsruhe Institute of Technology (KIT), Hermann-von-Helmholtz-Platz 1, Eggenstein-Leopoldshafen, 76344, Germany

HIGHLIGHTS

- Workflow for evaluating morphology evolution and mechanical properties in SOFCs.
- Decrease in effective elastic modulus due to microstructural coarsening.
- Elastic modulus decreases with pore volume fraction and increases with pore surface area.
- Critical volume fraction could be related to pore diameter, pore surface area, and TPB density.
- Coarsening is linked to electrochemical degradation and mechanical weakening.

ARTICLE INFO

Keywords:
Phase-field modeling
Stochastic modeling
Mechanical properties
Microstructural degradation

ABSTRACT

The microstructural degradation of Ni–CGO anodes in solid oxide fuel cells affects both electrochemical and mechanical properties. This study presents an automated workflow to quantify the evolution of geometrical descriptors and their influence on effective mechanical properties. Three-dimensional anode microstructures were aged up to 35,000 h using phase-field and stochastic modeling, followed by mechanical loading simulations. Aging caused microstructural coarsening as the mean pore diameter increased, while pore specific surface area and triple-phase boundary density decreased. Effective elastic moduli also decreased with aging. While the average von Mises stress remained nearly constant, the critical volume fraction increased with aging. Within the studied microstructures, the effective Hill modulus was strongly related to pore volume fraction and pore specific surface area. The critical volume fraction related positively with pore diameter and inversely with pore specific surface area and triple-phase boundary density.

1. Introduction

Motivation. Solid oxide fuel cells (SOFCs) are high-temperature electrochemical energy devices that efficiently convert fuel into electricity. Nickel/yttria-stabilized zirconia (Ni–YSZ) cermet anodes have been the state-of-the-art due to their good electrochemical performance and compatibility. Understanding how parameters like Ni/YSZ ratio, grain size, porosity, pore size distribution, tortuosity, and triple-phase boundary (TPB) density affect performance is key to optimizing these anodes [1]. However, Ni–YSZ anodes face challenges at lower operating temperatures (≈600 °C) because YSZ's ionic conductivity drops, leading to a high polarization resistance [2]. To enable efficient operation at intermediate temperatures (500–700 °C), alternative anode materials have emerged. In particular, nickel–gadolinium-doped ceria (Ni–CGO) cermet anodes have gained attention for intermediate-temperature SOFCs [3]. Gadolinium-doped ceria ($Ce_{0.9}Gd_{0.1}O_2$, CGO) offers higher ionic conductivity at these temperatures than YSZ and also exhibits mixed ionic-electronic conduction in reducing atmospheres [4]. This means

* Corresponding author.
Email addresses: ahmed.elmoghazy@kit.de (A. Elmoghazy), sabrina.weber@uni-ulm.de (S. Weber), ravi.jeela@partner.kit.edu (R.K. Jeela), andreas.prahs@kit.edu (A. Prahs), benedikt.prifling@uni-ulm.de (B. Prifling), daniel.schneider@kit.edu (D. Schneider), volker.schmidt@uni-ulm.de (V. Schmidt), britta.nestler@kit.edu (B. Nestler).

https://doi.org/10.1016/j.matdes.2026.116665
Received 10 May 2026; Received in revised form 19 July 2026; Accepted 23 July 2026
Available online 25 July 2026

that, unlike YSZ, the ceria phase can conduct both O^{2-} ions and electrons to some extent, so the fuel oxidation reaction is not limited to the narrow TPB regions, it can also occur on the broader CGO surface in the presence of gas (double-phase boundary of CGO and pore) [5]. Consequently, Ni–CGO anodes tend to have lower polarization resistance and high activity even at 600–700°C [4]. The mixed-conducting ceria phase also shows tolerance to sulfur poisoning and coking, improving durability in realistic fuel conditions [2].

Degradation mechanisms in Ni-based anodes. During operation, SOFC anodes undergo microstructural evolution that can degrade performance over time [6–8]. The Ni phase in Ni–CGO anodes is subject to similar degradation mechanisms as observed in Ni–YSZ anodes [9]. One primary mechanism is Ni coarsening (agglomeration) [2]. The Ni particles tend to sinter and grow in size under prolonged high-temperature reducing conditions. This coarsening reduces the overall Ni surface area and connectivity, and consequently diminishes the density of triple-phase boundary sites available for reaction [5]. For example, after long-term aging a Ni agglomeration can be observed, accompanied by a measurable decrease in TPB length density [10]. In Ni–CGO anodes aged for 240 hours at 800°C, the average Ni particle diameter was found to increase from 0.91 to 1.04 μm, with a corresponding drop in TPB density from 1.82 to 1.55 μm^{-2} [5].

Another major degradation mode is redox cycling damage. Nickel is highly susceptible to oxidation if air infiltrates the anode (e.g., during shutdown or fuel starvation) [11]. Upon oxidation to NiO, the Ni particles undergo a volumetric expansion of about 70% [12]. This large expansion/contraction during redox cycles imposes mechanical stresses that can crack the brittle ceramic scaffold and disrupt Ni–ceramic interfaces [13,14]. For example, a study of Ni–YSZ anodes (analogous in structure to Ni–CGO) showed that after 20 redox cycles the TPB length was reduced by ≈ 77% and new micro-cracks and pores had formed, contributing to a decrease in the hardness and the elastic modulus by 62% and 45%, respectively [13]. It should be noted that this study focuses only on isothermal degradation due to particle coarsening, and not on redox cycling damage.

Studies on mechanical properties of Ni-based anodes. The anode is part of the load-bearing structure in many SOFC designs (especially anode-supported cells and metal-supported cells). Changes in its microstructure can affect its overall mechanical properties [15,16]. Despite extensive work on electrochemical performance and microstructural evolution in Ni–CGO anodes, direct, time-resolved measurements of the degradation of mechanical properties under steady, isothermal aging remain scarce. The few Ni–CGO mechanical datasets that do exist are either single-state characterizations or geometry-specific tests: micro-/nano-indentation on Ni–CGO anode pellets and burst tests on NiO–CGO micro-tubes [17], biaxial flexure of electrolyte-supported laminates showing a strength drop when a NiO/CGO fuel electrode is added [18], flexural strength of NiO–CGO anode-supported cells fabricated by gel-casting [19], and in-situ synchrotron X-ray diffraction on Ni–CGO cermets that reveal lattice-scale thermo-mechanical behavior [20]. Designs emphasizing redox robustness of Ni–CGO also report improved mechanical stability under cycling, but these works target redox damage rather than isothermal coarsening [21]. Computational studies using reconstructed Ni–YSZ microstructures and porous-media models have further confirmed that elastic moduli decrease as porosity increases, consistent with Gibson–Ashby scaling laws [22–24]. To the best of our knowledge, no study has systematically tracked the directional elastic moduli or stress localization metrics of Ni–CGO as a function of isothermal aging time.

Originality. The literature establishes that Ni–CGO based anodes undergo microstructural degradation (e.g., Ni coarsening, TPB loss) and that the mechanical and electrochemical properties are generally strongly influenced by porosity and microstructural connectivity [25–27]. However, few studies have investigated how the elastic modulus of Ni–CGO anodes degrades with isothermal aging, whether it exhibits anisotropy, and how mechanical reliability metrics (e.g., stress distribution) correlate with evolving geometric descriptors. This study aims to fill this gap in the literature by introducing a workflow that is capable of calculating different geometrical descriptors and effective mechanical properties.

Objective. In this study, we present a workflow implemented in Kadi4Mat [28,29] to analyze aging Ni–CGO microstructures and quantify both geometrical and mechanical descriptors during aging. The study is based on one experimentally derived Ni–CGO microstructure, which is aged using the phase-field method [30–32] and complemented with stochastic microstructures generated from the same calibrated aging trajectory [33]. The phase-field method is used to simulate the physical mechanisms associated with isothermal coarsening, while the stochastic model provides realization-to-realization variability around the calibrated morphology. The scope of this work is to establish and demonstrate a reproducible workflow for coupling microstructure aging, descriptor calculation, and mechanical-property evaluation.

The workflow calculates phase radii distributions, specific surface areas, double-phase boundary density, TPB density, and volume fractions. Furthermore, mechanical properties such as directional elastic moduli, the Hill average elastic modulus, von Mises stress distributions, and the critical volume fraction are calculated. By comparing the temporal evolution of these descriptors, the workflow enables the identification of potential microstructure–property relationships within the investigated dataset. Such relationships can provide insight into how coarsening-induced morphological changes affect mechanical degradation and may serve as a basis for future electrode optimization studies involving broader variations in composition, particle-size distribution, and statistically independent initial microstructures.

Outline. In Section 2 the numerical models used to produce the aged microstructures are presented. The workflow is outlined and described in Section 3. The simulation studies and their results are discussed in Section 4. Concluding remarks are given in Section 5.

2. Numerical models

2.1. Physics-based simulations

Multiphase-field model. A modeling approach is employed to capture the essential physical mechanisms of coarsening in Ni-CGO anodes, while maintaining computational efficiency. The model is based on the following assumptions: conservation of mass and volume, isotropic interfacial properties, as well as surface and interfacial diffusion as dominant mass transport pathways. Both Ni and CGO coarsening are considered primary degradation processes. Accordingly, this study focuses only on determining the effects of Ni and CGO coarsening on the microstructural evolution of the anode and, consequently, on the long-term performance of SOFCs.

A multiphase-field model centered on the grand-potential functional [34] together with a recent extension that accounts for surface self-diffusion [35], is adopted to model the coarsening phenomena of nickel and CGO. The model formulation includes the grand-potential functional Ω of the system with volume V, dependent on the order parameters $\boldsymbol{\phi} = \{\phi_1, \phi_2, \dots, \phi_N\}$ of N phases and the volumetric chemical potentials $\boldsymbol{\mu} = \{\mu_1, \mu_2, \dots, \mu_{K-1}\}$ of $K-1$ components and reads

$$\Omega(\boldsymbol{\phi}, \boldsymbol{\nabla\phi}, \boldsymbol{\mu}) = \int_V \frac{1}{\epsilon} w(\boldsymbol{\phi}) + \epsilon a(\boldsymbol{\nabla\phi}) + \psi(\boldsymbol{\phi}, \boldsymbol{\mu}) \, \mathrm{d}V. \tag{1}$$

Here, $w(\boldsymbol{\phi})$, $a(\boldsymbol{\nabla\phi})$ and $\psi(\boldsymbol{\phi}, \boldsymbol{\mu})$ represent the potential, gradient and bulk terms respectively. With the scalar parameter ϵ, the length scale is controlled and determines the diffuse interface width $\delta = \epsilon\pi^2/4$. The combined potential and gradient expressions according to the notation of [36] include the interfacial energy in the model and stabilize the

interfacial profile with a finite thickness. The gradient term [30] is expressed as

$$a(\nabla\boldsymbol{\phi}) = -\sum_{\beta=2}^{N}\sum_{\alpha=1}^{\beta-1}\gamma_{\alpha\beta}\nabla\phi_\alpha\cdot\nabla\phi_\beta, \tag{2}$$

where $\gamma_{\alpha\beta}$ denotes the interfacial energy between phases α and β. An obstacle potential of the following form is chosen as

$$w(\boldsymbol{\phi}) = \begin{cases} \dfrac{16}{\pi^2}\displaystyle\sum_{\beta=2}^{N}\sum_{\alpha=1}^{\beta-1}\gamma_{\alpha\beta}\,\phi_\alpha\phi_\beta, & \boldsymbol{\phi}\in\mathcal{G}, \\ \infty, & \boldsymbol{\phi}\notin\mathcal{G}, \end{cases} \tag{3}$$

with Gibbs simplex $\mathcal{G} = \left\{\boldsymbol{\phi}\,|\,\sum_{\alpha=1}^{N}\phi_\alpha = 1 \wedge \phi_\alpha \geq 0\right\}$.

Furthermore, the bulk grand-potential density is expressed as the interpolation of the grand-potential densities of the individual phases, i.e., $\psi(\boldsymbol{\phi},\boldsymbol{\mu}) = \sum_{\alpha=1}^{N}\psi^\alpha(\boldsymbol{\mu})\mathrm{h}_\alpha(\boldsymbol{\phi})$. The grand-potential density for phase α is given as

$$\psi^\alpha(\boldsymbol{\mu}) = f^\alpha(c^\alpha(\boldsymbol{\mu})) - \sum_{i=1}^{K-1}\mu_i c_i^\alpha(\boldsymbol{\mu}), \quad \forall\alpha\in\{1,\ldots,\mathrm{N}\}, \tag{4}$$

where f^α is the bulk free energy of phase α and depends on the phase-specific compositions $c^\alpha = \{c_1^\alpha, c_2^\alpha, \ldots, c_{\mathrm{K}-1}^\alpha\}$.

For phase α, the free energy is written as the sum of the individual energetic contributions of the conserved species, $f^\alpha(c^\alpha(\boldsymbol{\mu})) = \sum_{i=1}^{K-1} f_i^\alpha(c_i^\alpha)$. In the present Ni–CGO system, the solid phases are treated as nearly pure phases with fixed equilibrium compositions. Therefore, the individual free-energy contributions are approximated by parabolic functions,

$$f_i^\alpha(c_i^\alpha) = A_i\left[c_i^\alpha(\mu_i) - c_{i,\mathrm{eq}}^\alpha\right]^2, \qquad i\in\{\mathrm{Ni},\mathrm{CGO}\}. \tag{5}$$

Here, A_i is a thermodynamic prefactor controlling the energetic penalty for deviations from the equilibrium composition and thereby the strength of the immiscibility between the phases. The values of A_i are chosen sufficiently large to maintain volume conservation of the individual phases during coarsening. The quantity $c_{i,\mathrm{eq}}^\alpha$ denotes the equilibrium concentration of species i in phase α. A local quasi-equilibrium assumption is used, where the condition

$$\mu_i = \frac{\partial f^\alpha(c^\alpha)}{\partial c_i^\alpha} = \frac{\partial f^\beta(c^\beta)}{\partial c_i^\beta} = \frac{\partial f^N(c^N)}{\partial c_i^N} \tag{6}$$

is met. The evolution of the chemical potential is given as

$$\frac{\partial\mu_i(\boldsymbol{x},t)}{\partial t} = \left[\sum_{\alpha=1}^{N}h_\alpha(\boldsymbol{\phi})\frac{\partial c_j^\alpha(\boldsymbol{\mu})}{\partial\mu_i}\right]^{-1}\left[\frac{\partial c_j(\boldsymbol{x},t)}{\partial t} - \sum_{\alpha=1}^{N}c_j^\alpha(\boldsymbol{\mu})\frac{\partial h_\alpha(\boldsymbol{\phi}(\boldsymbol{x},t))}{\partial t}\right]. \tag{7}$$

Following [30], the evolution equation of each phase-field ϕ_α is stated as

$$\epsilon\frac{\partial\phi_\alpha(x,t)}{\partial t} = \frac{1}{\tilde{N}}\sum_{\beta\neq\alpha}^{N}m_{\alpha\beta}\left(\frac{\delta\Omega}{\delta\phi_\beta} - \frac{\delta\Omega}{\delta\phi_\alpha}\right), \tag{8}$$

where $\tilde{N}$ denotes the local number of phases, and the terms $\delta/(\delta\phi_\alpha)$ and $\delta/(\delta\phi_\beta)$ correspond to the variational derivative with respect to ϕ_α and ϕ_β. Furthermore, $m_{\alpha\beta}$ (in $\mathrm{m}^4/(\mathrm{J}\cdot\mathrm{s})$) indicates the interface mobility of phases α and β, which is defined as the kinetic coefficient controlling the rate of the phase-field evolution at the diffuse interface between the phases α and β. It is distinct from the chemical mobilities used for surface and interfacial diffusion, which govern the conserved mass transport during coarsening (introduced below). In the present simulations, $m_{\alpha\beta}$ was chosen such that interface attachment kinetics does not become the rate-limiting mechanism, so that the coarsening evolution is governed by surface diffusion and interfacial diffusion along the Ni–CGO interface. This condition is satisfied by ensuring the characteristic length scale associated with the attachment kinetics, defined as ($l_c = \sqrt{B/(\gamma_{\alpha\beta}\,m_{\alpha\beta})}$) being much smaller than the diffuse interfacial width, i.e., ($l_c \ll \pi^2\epsilon/4$) [35].

Three distinct order parameters $\boldsymbol{\phi} = \{\phi_{Ni}, \phi_{CGO}, \phi_{Pore}\}$ representing the nickel phase, the CGO phase, and the pore phase, respectively, are employed to model the porous Ni-CGO system. A set of two dimensionless composition variables $\boldsymbol{c} = \{c_{\mathrm{Ni}}, c_{\mathrm{CGO}}\}$ (mole fractions) with the composition of the porous phase $c_{\mathrm{Pore}} = 1 - c_{\mathrm{Ni}} - c_{\mathrm{CGO}}$ enables the transport of each substance. The dimensionless, conserved composition fields evolve according to the conservation laws governing the system, expressed as

$$\frac{\partial c_i(\boldsymbol{x},t)}{\partial t} = -\nabla\cdot\boldsymbol{j}_i, \quad i = 1,\ldots,K-1 \tag{9}$$

in which $\boldsymbol{j}_i$ refers to the flux of the species i. Surface diffusion is typically assumed to be the dominant mechanism for mass transfer [10]; however, in contrast to Ni-YSZ anodes, Ni-CGO anodes show coarsening behavior for both Ni and CGO during isothermal aging. In that regard, this model incorporates both surface diffusion as well as diffusion along the interface between Ni and CGO. The flux density of Ni is given as

$$\boldsymbol{j}_{Ni} = -\frac{32}{\pi^2\varepsilon}\nabla\mu_{\mathrm{Ni}}(M_{\mathrm{Ni}}^{\mathrm{NiPore}}\phi_{\mathrm{Ni}}\phi_{\mathrm{Pore}} + M_{\mathrm{Ni}}^{\mathrm{NiCGO}}\phi_{\mathrm{Ni}}\phi_{\mathrm{CGO}}), \tag{10}$$

where $M_{\mathrm{Ni}}^{\mathrm{NiPore}}$ and $M_{\mathrm{Ni}}^{\mathrm{NiCGO}}$ are mobilities of Ni along the tangential direction of the free nickel surface and along the Ni/CGO interface respectively. These mobilities are directly related to the surface self-diffusivity $D_{\mathrm{Ni}}^{\mathrm{NiPore}}$ and the interfacial self-diffusivity $D_{\mathrm{Ni}}^{\mathrm{NiCGO}}$ by

$$M_{\mathrm{Ni}}^{\mathrm{NiPore}} = \frac{D_{\mathrm{Ni}}^{\mathrm{NiPore}}\delta_s V_m(\Delta c_{\mathrm{Ni,eq}}^{\mathrm{Ni-Pore}})^2}{RT}, \tag{11a}$$

$$M_{\mathrm{Ni}}^{\mathrm{NiCGO}} = \frac{D_{\mathrm{Ni}}^{\mathrm{NiCGO}}\delta_I V_m(\Delta c_{\mathrm{Ni,eq}}^{\mathrm{Ni-CGO}})^2}{RT}. \tag{11b}$$

Here, δ_s and δ_I are the atomistic thicknesses of the surface and the interface respectively, V_m is the molar volume, R is the ideal gas constant, and T is the temperature. The model-specific composition differences $\Delta c_{\mathrm{Ni,eq}}^{\mathrm{Ni-Pore}}$ and $\Delta c_{\mathrm{Ni,eq}}^{\mathrm{Ni-CGO}}$ are defined as $\Delta c_{\mathrm{Ni,eq}}^{\mathrm{Ni-Pore}} = c_{\mathrm{Ni,eq}}^{\mathrm{Ni}} - c_{\mathrm{Ni,eq}}^{\mathrm{Pore}} = 0.8$ and $\Delta c_{\mathrm{Ni,eq}}^{\mathrm{Ni-CGO}} = c_{\mathrm{Ni,eq}}^{\mathrm{Ni}} - c_{\mathrm{Ni,eq}}^{\mathrm{CGO}} = 0.8$, respectively. The same formulations apply to CGO.

At the domain boundaries, zero-flux boundary conditions are imposed, whereby the boundaries are treated as isolating (i.e., $\boldsymbol{j_i}\cdot\boldsymbol{n} = 0\forall i,\ x\in\mathrm{d}V$), with $\boldsymbol{n}$ denoting the normal to the domain boundary, implying no net flux across the boundary. Also, a perpendicular contact condition is assumed for the order parameters ($\nabla\phi_\alpha\cdot\boldsymbol{n} = 0$), which ensures boundary normality of the order parameter gradient. A SIMD-vectorized (Single Instruction, Multiple Data) solver is used for the multiphase-field simulations, the implementation of which is described in detail in Section 4.2 of [37]. A summary of the main parameters used in the multiphase-field simulations is given in Table 1.

Further details on the validation of the multiphase-field simulation results against experimental data of Ni-CGO anodes aged for 240 h, 1100 h and the model parameters, representing the operating conditions of Ni-CGO at 900 °C under a gas composition of H_2-50% / H_2O-50% can be found in [5,38].

Solid mechanics formulation within the MPFM framework. The temporal evolution of the elastic mechanical properties due to isothermal aging is one of the main objectives of the present work. Load simulations are therefore carried out on the aged microstructures at distinct time

Table 1
Model parameters used in the multiphase-field simulations, adopted from [38].

Parameter (symbol)	Value (units)
Ni surface chemical mobility $\left(M_{\mathrm{Ni}}^{\mathrm{NiPore}}\right)$	1.73×10^{-31} m^6/(J s)
Ni chemical mobility along the Ni/CGO interface $\left(M_{\mathrm{Ni}}^{\mathrm{NiCGO}}\right)$	1.73×10^{-36} m^6/(J s)
CGO surface chemical mobility $\left(M_{\mathrm{CGO}}^{\mathrm{CGOPore}}\right)$	7.55×10^{-36} m^6/(J s)
CGO chemical mobility along the Ni/CGO interface $\left(M_{\mathrm{CGO}}^{\mathrm{NiCGO}}\right)$	1.73×10^{-42} m^6/(J s)
Interfacial energy Ni/pore $\left(\gamma_{\mathrm{NiPore}}\right)$	2.10 J/m^2
Interfacial energy Ni/CGO $\left(\gamma_{\mathrm{NiCGO}}\right)$	2.43 J/m^2
Interfacial energy CGO/pore $\left(\gamma_{\mathrm{CGOPore}}\right)$	1.43 J/m^2
Interface mobility Ni/pore $\left(m_{\mathrm{NiPore}}\right)$	6.92×10^{-17} m^4/(J s)
Interface mobility Ni/CGO $\left(m_{\mathrm{NiCGO}}\right)$	6.92×10^{-17} m^4/(J s)
Interface mobility CGO/pore $\left(m_{\mathrm{CGOPore}}\right)$	6.92×10^{-17} m^4/(J s)
Interface width parameter (ϵ)	100 nm
Thermodynamic prefactor for Ni $\left(A_{\mathrm{Ni}}\right)$	2.1×10^{8} J/m^3
Thermodynamic prefactor for CGO $\left(A_{\mathrm{CGO}}\right)$	2.1×10^{9} J/m^3
Equilibrium composition of Ni in Ni $\left(c_{\mathrm{Ni,eq}}^{\mathrm{Ni}}\right)$	90 mol%
Equilibrium composition of Ni in CGO $\left(c_{\mathrm{Ni,eq}}^{\mathrm{CGO}}\right)$	10 mol%
Equilibrium composition of Ni in pore $\left(c_{\mathrm{Ni,eq}}^{\mathrm{Pore}}\right)$	10 mol%
Equilibrium composition of CGO in Ni $\left(c_{\mathrm{CGO,eq}}^{\mathrm{Ni}}\right)$	10 mol%
Equilibrium composition of CGO in CGO $\left(c_{\mathrm{CGO,eq}}^{\mathrm{CGO}}\right)$	90 mol%
Equilibrium composition of CGO in pore $\left(c_{\mathrm{CGO,eq}}^{\mathrm{Pore}}\right)$	10 mol%
Atomistic thickness of the surface (δ_s)	0.1 nm
Atomistic thickness of the interface (δ_I)	0.1 nm

increments. In this regard, a quasi-static, small-strain solid mechanics formulation is employed, and body forces are neglected. The mechanical response is assumed to be linear elastic, so that the calculated stresses represent the instantaneous elastic response of the microstructure under the prescribed boundary conditions and thermal-expansion mismatch. Time-dependent relaxation mechanisms such as creep, viscoplasticity, interfacial sliding, damage evolution, and fracture are not included. This assumption enables a consistent comparison of the relative influence of coarsening-induced morphological changes on the effective stiffness and stress localization, but the resulting local stress values should not be interpreted as long-term residual stresses under SOFC operating conditions. At elevated operating temperatures, stress relaxation may reduce local stress concentrations over time [39].

The balance of linear momentum is therefore expressed as

$$\operatorname{div}\left(\overline{\boldsymbol{\sigma}}\right)=\mathbf{0},\quad \overline{\boldsymbol{\sigma}}=\sum_{\alpha=1}^{N^*}\phi_\alpha\boldsymbol{\sigma}^\alpha, \tag{12}$$

cf. [40], where $\overline{\boldsymbol{\sigma}}$ denotes the interpolated Cauchy stress calculated from the phase-specific stresses $\boldsymbol{\sigma}^\alpha$, and ϕ_α represents the order parameter of phase α. The infinitesimal strain tensor $\boldsymbol{\varepsilon}$ is interpolated analogously as

$$\boldsymbol{\varepsilon}=\sum_{\alpha=1}^{N^*}\phi_\alpha\boldsymbol{\varepsilon}^\alpha. \tag{13}$$

Following the jump condition approach [41–43], the local phase strain $\boldsymbol{\varepsilon}^\alpha$ can be written as

$$\boldsymbol{\varepsilon}^\alpha=\boldsymbol{\varepsilon}+\sum_{\beta=1,\beta\neq\alpha}^{N^*}\phi_\beta\llbracket\boldsymbol{\varepsilon}\rrbracket^{\alpha\beta}, \tag{14}$$

where $\llbracket\boldsymbol{\varepsilon}\rrbracket^{\alpha\beta}$ denotes the strain jump across diffuse interfaces between phases α and β given by $\llbracket\boldsymbol{\varepsilon}\rrbracket^{\alpha\beta}=\boldsymbol{\varepsilon}^\alpha-\boldsymbol{\varepsilon}^\beta$. Under the small strain assumption, the phase-specific strain $\boldsymbol{\varepsilon}^\alpha$ is decomposed additively into an elastic part $\boldsymbol{\varepsilon}^{\mathrm{el},\alpha}$ and a thermal expansion contribution $\boldsymbol{\varepsilon}^{\theta,\alpha}$,

$$\boldsymbol{\varepsilon}^\alpha=\boldsymbol{\varepsilon}^{\mathrm{el},\alpha}+\alpha_\theta^\alpha\Delta\theta\boldsymbol{I}, \tag{15}$$

with α_θ^α being the isotropic coefficient of thermal expansion of phase α, $\Delta\theta$ the temperature difference with respect to the reference temperature ($\Delta\theta=\theta-\theta_{\mathrm{ref}}^\alpha$), and $\boldsymbol{I}$ the second-order identity tensor.

Table 2
Material properties of the individual phases used in the mechanical simulations.

Phase	Elastic modulus E (GPa)	Poisson's ratio ν	Thermal expansion α_θ (K^{-1})
Ni	200 [44]	0.31 [44]	16.00×10^{-6} [45]
CGO	120 [46]	0.33 [46]	12.96×10^{-6} [47]

The corresponding phase-specific stresses follow from Hooke's law in each phase,

$$\boldsymbol{\sigma}^\alpha=\mathbb{C}^\alpha\left[\boldsymbol{\varepsilon}^{\mathrm{el},\alpha}\right]=\mathbb{C}^\alpha\left[\boldsymbol{\varepsilon}^\alpha-\boldsymbol{\varepsilon}^{\theta,\alpha}\right], \tag{16}$$

where $\mathbb{C}^\alpha$ denotes the phase-specific stiffness tensor. Assuming isotropic elasticity for each phase, it is expressed as

$$\mathbb{C}^\alpha=3K^\alpha\mathbb{P}_1+2G^\alpha\mathbb{P}_2, \tag{17}$$

with K^α and G^α representing the bulk and shear moduli, respectively. The projection tensors are defined as $\mathbb{P}_1=1/3\boldsymbol{I}\otimes\boldsymbol{I}$ and $\mathbb{P}_2=\mathbb{I}^{\mathrm{S}}-\mathbb{P}_1$ where $\mathbb{I}^{\mathrm{S}}$ is the symmetric fourth-order identity tensor.

In the mechanical simulations, the pore phase was assigned a small finite elastic stiffness of $E_{\mathrm{pore}}=1$ Pa and $\nu_{\mathrm{pore}}=0.33$ to avoid singularities in the stiffness matrix. Since this stiffness is several orders of magnitude lower than the stiffness of Ni and CGO, the pore phase contributes negligibly to the load-bearing response and acts mechanically as a near-void phase. The material properties used in this study are shown in Table 2.

2.2. Stochastic simulations

Overview of the stochastic microstructure model. In this section, the stochastic microstructure model of [33] is briefly introduced. Therefore, two stochastically independent and motion invariant Gaussian random fields $\{X(t),t\in\mathbb{R}^3\}$ and $\{Y(t),t\in\mathbb{R}^3\}$ with covariance functions $\rho_X,\rho_Y:[0,\infty)\to\mathbb{R}$ are used. More precisely, the covariance functions are assumed to be $\rho_X(h)=\exp(-(\alpha_X h)^{\beta_X})$ and $\rho_Y(h)=\exp(-(\alpha_Y h)^{\beta_Y})$ for $h>0$, where $\alpha_X,\alpha_Y\in(0,\infty)$ and $\beta_X,\beta_Y\in(0,2)$ [48]. In addition, we assume that X and Y are standardized, i.e., we assume that $\mathbb{E}X(t)=\mathbb{E}Y(t)=0$ and $Var(X(t))=Var(Y(t))=1$ for all $t\in\mathbb{R}^3$ However, a Gaussian random field is not suitable to accurately model the nickel phase of the considered SOFC anodes. That is why a χ^2-field $\{Z(t),t\in\mathbb{R}^3\}$ with two degrees of freedom based on the Gaussian field X is used. Formally, it holds $Z(t)=X_1^2(t)+X_2^2(t)$ for all $t\in\mathbb{R}^3$, where X_1 and X_2 are two independent copies of X. The covariance function of Z is then given by $\rho_Z(h)=4\rho_X(h)^2$ for all $h>0$ [49]. The two random fields Z and Y are used to model the three phases with so-called excursion sets [50]. Therefore, the two threshold parameters $\lambda_Z,\lambda_Y\in\mathbb{R}$ are used. More precisely, the model is given by

$$\Xi_{\mathrm{Ni}}=\{t\in\mathbb{R}^3:Z(t)\geq\lambda_Z\},$$
$$\Xi_{\mathrm{P}}=\mathrm{cl}(\{t\in\mathbb{R}^3:Y(t)\geq\lambda_Y\}\cap\Xi_{\mathrm{Ni}}^{\complement}),$$
$$\Xi_{\mathrm{CGO}}=\mathrm{cl}((\Xi_{\mathrm{Ni}}\cup\Xi_{\mathrm{P}})^{\complement}),$$

where cl denotes the topological closure and $\complement$ denotes the complement of a set. Note that the set Ξ_{Ni} models the nickel phase, while Ξ_{CGO} and Ξ_{P} model the CGO phase and pore space, respectively.

Parameters of the stochastic microstructure model. This stochastic microstructure model exhibits a six-dimensional parameter vector $\theta=(\lambda_Z,\lambda_Y,\alpha_X,\alpha_Y,\beta_X,\beta_Y)$, which is fitted with analytical formulas to the 3D microstructure obtained from the phase-field model simulations. More details on the fitting procedure can be found in [33]. Afterwards, an exponential regression is performed on each model parameter evolution over time, to obtain a time-dependent 3D microstructure model;

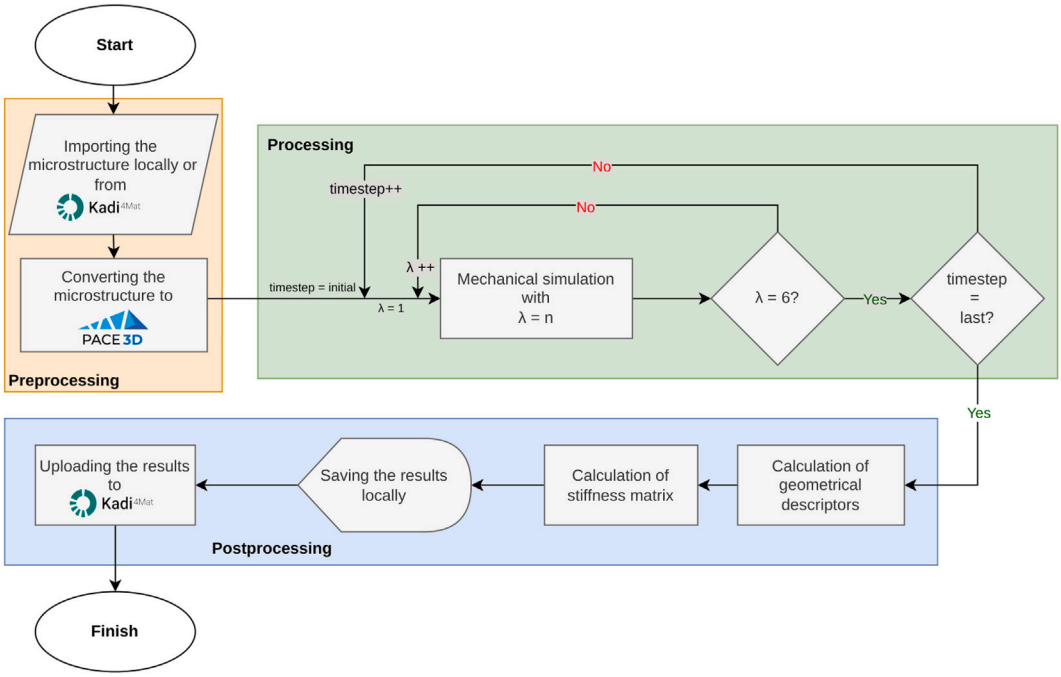

Fig. 1. Schematic representation of the workflow, implemented and used in this work, to run the mechanical simulations, calculate the geometrical descriptors and determine the effective mechanical properties.

see [33]. This time-dependent model is used to generate time series of the 3D microstructure of SOFC anodes. To ensure the continuity of the model realizations over time, a random seed is chosen and fixed afterwards for the entire time series. By setting a specific seed value, the pseudo-random number generator is initialized with a defined starting point, resulting in an identical sequence of random numbers each time the code is executed. Thus, the change in the microstructure over time is only influenced by the change in the model parameters.

3. Workflow

Overview. The workflow was implemented in KadiStudio, the workflow editor of the Kadi4Mat research data infrastructure. KadiStudio enables the design of modular, automated workflows that adhere to FAIR (Findable, Accessible, Interoperable, Reusable) data principles [29,51]. A schematic overview of the developed workflow is shown in Fig. 1, while the implementation in KadiStudio is illustrated in Fig. A.1.

The workflow begins with importing anode microstructures, either from local storage or directly from the Kadi4Mat repository. After preprocessing, the microstructures are prepared for mechanical load simulations, which provide the effective stiffness and other effective properties. Subsequently, geometrical descriptors and performance-related metrics are computed. The resulting datasets are stored locally and uploaded to Kadi4Mat, ensuring long-term accessibility and reproducibility. This procedure is repeated for all microstructures under investigation.

3.1. Pre- and processing nodes

Preprocessing. The pre-processing stage of the workflow manages the import, preparation, and format conversion of microstructures for subsequent analysis. As illustrated in Fig. 1, the input nodes can access data from multiple sources, including local directories and the Kadi4Mat repository. The input data can include both aged and pristine microstructures.

Since the subsequent mechanical and geometrical analyses are executed the workflow manages the import within the Phase-field Algorithms for Computational Engineering (PACE3D) [52] environment,[1] each imported dataset must first be converted to the PACE3D format. This is accomplished through a Python-based conversion script that reads the original data, typically provided as `.npy` arrays or `.tiff` image stacks, and transforms them into scalar fields compatible with the PACE3D software. During this step, the corresponding simulation input files are also generated automatically, defining the material parameters, phase identifiers, and boundary conditions required for the mechanical load simulations that follow.

Processing nodes. Once pre-processing is complete, the workflow advances to the processing stage, where the converted microstructures and their associated input files are passed to simulation nodes that perform the mechanical load calculations. For each aged microstructure, a loop over the temporal frames is executed, and within each frame, six independent uniaxial loading cases ($\lambda = 1, \ldots, 6$) are applied sequentially to compute the anisotropic elastic response of the material. An additional loading case is performed to extract further mechanical characteristics relevant to this study, such as the average von Mises stress and the critical volume fraction (Eq. 28). All simulations are performed using the PACE3D software. These simulations act as the basis for all subsequent analyses.

3.2. Post-processing nodes

Geometrical descriptors. The workflow integrates methods to compute geometric descriptors of the microstructure, such as phase volume fractions, median particle diameter from the continuous particle size distribution, specific surface areas (SSAs), and triple phase boundary (TPB) density. Particle sizes are quantified using the continuous sphere-fitting method following Münch and Holzer [53], which fills the phase volume with overlapping spheres of varying diameters. This technique has been used successfully in experimental measurements of SOFC anodes [54]. It provides the cumulative distribution that decreases from unity to zero as sphere diameter increases. The median particle size (d_{50}) is then defined

[1] Formerly named as Parallel Algorithms for Crystal Evolution in 3D.

at the 50% point of the cumulative distribution. TPB density is determined by a skeletonization algorithm that identifies intersection voxels, reduces them to a one-voxel-thick network, and smooths the resulting skeleton to minimize discretization effects [55]. The SSA, A_α of a given phase α, is evaluated from its order parameter field ϕ_α by integrating the magnitude of its gradient over the simulation volume, i.e.,

$$A_\alpha = \frac{1}{V}\int_V |\nabla \phi_\alpha|\, dV, \tag{18}$$

where V denotes the total volume. From these quantities, the interfacial areas $A_{\alpha-\beta}$ between different phase pairs (α, β) can be obtained by solving a linear system that relates the total surface area of each phase to the sum of its pairwise interfaces. For example, in a three-phase system consisting of Ni, CGO, and pores, the relations

$$A_{\text{Ni}} = A_{\text{Ni-Pore}} + A_{\text{Ni-CGO}}, \tag{19a}$$

$$A_{\text{CGO}} = A_{\text{CGO-Pore}} + A_{\text{Ni-CGO}}, \tag{19b}$$

$$A_{\text{Pore}} = A_{\text{Ni-Pore}} + A_{\text{CGO-Pore}}, \tag{19c}$$

hold. Particular emphasis is placed on the CGO–pore interface. Owing to the mixed ionic–electronic conductivity of CGO, the entire CGO surface in contact with pores can participate in electrochemical reactions, making this descriptor highly relevant for electrical performance. All methods were implemented within the PACE3D framework and validated against established benchmarks [56].

Method of obtaining the directional elastic moduli. Since the fully resolved microstructure is available, a numerical homogenization is preferred over analytical mean field methods [57]. In this regard, the effective stiffness tensor $\bar{\mathbb{C}}$ is obtained by a strain-controlled numerical homogenization scheme based on six independent macroscopic load cases corresponding to the 6 components of the normed Voigt notation [58]. I.e., for $\lambda = 1, \dots, 6$, a prescribed macroscopic strain $\bar{\boldsymbol{\varepsilon}}^\lambda$ is imposed, such that $\mathbf{u} = \bar{\boldsymbol{\varepsilon}}^\lambda \boldsymbol{x} \in \delta\Omega$ holds true. For example, for $\lambda = 1$, the corresponding macroscopic strain is given by $\bar{\boldsymbol{\varepsilon}}^1 = \varepsilon_0\, \mathbf{e}_1 \otimes \mathbf{e}_1$, with the strain amplitude ε_0 in the 11 direction. In this work, a strain amplitude $\varepsilon_0 = 0.001$ is chosen in order to remain within the constraints of the small strain assumption. The corresponding boundary value problem of linear elasticity is solved yielding the stress field $\boldsymbol{\sigma}^\lambda(\mathbf{x})$. The volume-averaged macroscopic stress response is then computed as

$$\langle \boldsymbol{\sigma}^\lambda \rangle = \frac{1}{V}\int_V \boldsymbol{\sigma}^\lambda(\mathbf{x})\, dV. \tag{20}$$

The homogenized constitutive relation can be expressed as $\langle \boldsymbol{\sigma}^\lambda \rangle = \bar{\mathbb{C}}\, \bar{\boldsymbol{\varepsilon}}^\lambda$. For the numerical homogenization scheme, the normed Voigt notation is used. To extract the stiffness contributions from each load case, both sides are multiplied by $\left(\underline{\bar{\varepsilon}^\lambda}\right)^T$ and normalized by $\left(\underline{\bar{\varepsilon}^\lambda}\right)^T \underline{\bar{\varepsilon}^\lambda}$, with $\underline{\bar{\varepsilon}^\lambda}$ denoting the Voigt representation of $\bar{\boldsymbol{\varepsilon}}^\lambda$. This removes the dependence on the chosen strain amplitude ε_0 and yields

$$\underline{\underline{\bar{C}}}^\lambda = \frac{\langle \sigma^\lambda \rangle \left(\underline{\bar{\varepsilon}^\lambda}\right)^T}{\left(\underline{\bar{\varepsilon}^\lambda}\right)^T \underline{\bar{\varepsilon}^\lambda}}. \tag{21}$$

Here, $\underline{\underline{\bar{C}}}$ denotes the matrix representation of the stiffness tensor $\mathbb{C}$ in normed Voigt notation. In this context, $\underline{\underline{\bar{C}}}^\lambda$ refers to the matrix representation of the λth column of $\underline{\underline{\bar{C}}}$ obtained by evaluating Eq. (21). Thus, each $\underline{\underline{\bar{C}}}^\lambda$ corresponds to a partial stiffness matrix that contributes a single column to $\bar{\mathbb{C}}$. For example, if the applied strain is $\underline{\bar{\varepsilon}}^1 = [\,\varepsilon_0,\ 0,\ 0,\ 0,\ 0,\ 0\,]^\mathsf{T}$, then the averaged stress response $\langle \underline{\sigma}^1 \rangle$ provides the first column of $\bar{\mathbb{C}}$. Analogously, shear load cases with $\underline{\bar{\varepsilon}^\lambda}$ nonzero in only one shear component contribute the corresponding shear columns, with the conventional $\sqrt{2}$ normalization [59].

The complete effective stiffness tensor is finally assembled as the sum of the contributions from the six load cases, i.e.,

$$\underline{\underline{\bar{C}}} = \sum_{\lambda=1}^{6} \underline{\underline{\bar{C}}}^\lambda. \tag{22}$$

Following Böhlke and Brüggemann [60], the elastic modulus body can be plotted from the homogenized stiffness tensor and the directional elastic moduli can be extracted therefrom [60] using

$$\frac{1}{E(\mathbf{d})} = \mathbf{d} \otimes \mathbf{d} \cdot \mathbb{S}[\mathbf{d} \otimes \mathbf{d}], \tag{23}$$

where $\mathbf{d}$ is the normalized direction vector and $\mathbb{S}$ is the compliance matrix. This allows the calculation of the elastic moduli of any microstructure regardless of the material symmetry group.

In addition to these directional values, an isotropic equivalent modulus was computed by projecting the anisotropic tensor onto isotropic Voigt and Reuss bounds and averaging them in the sense of Hill [61]. The Voigt estimates for bulk and shear moduli are

$$K_{Voigt} = \frac{C_{11} + C_{22} + C_{33} + 2(C_{12} + C_{13} + C_{23})}{9}, \tag{24a}$$

$$G_{Voigt} = \frac{C_{11} + C_{22} + C_{33} - (C_{12} + C_{13} + C_{23}) + 3(C_{44} + C_{55} + C_{66})}{15}. \tag{24b}$$

While the Reuss bounds follow from the compliance tensor as

$$\frac{1}{K_{Reuss}} = S_{11} + S_{22} + S_{33} + 2(S_{12} + S_{13} + S_{23}), \tag{25a}$$

$$\frac{1}{G_{Reuss}} = \frac{4}{15}\left(S_{11} + S_{22} + S_{33} - S_{12} - S_{13} - S_{23}\right) + \frac{3}{15}(S_{44} + S_{55} + S_{66}). \tag{25b}$$

The Hill averages are then

$$K_{Hill} = \tfrac{1}{2}(K_{Voigt} + K_{Reuss}), \qquad G_{Hill} = \tfrac{1}{2}(G_{Voigt} + G_{Reuss}), \tag{26}$$

the effective isotropic elastic modulus is obtained as

$$E_{Hill} = \frac{9 K_{Hill} G_{Hill}}{3K_{Hill} + G_{Hill}}. \tag{27}$$

It should be noted that these Voigt–Reuss–Hill estimates provide an isotropic projection of the generally anisotropic effective stiffness tensor, and are therefore used here only as scalar indicators to compare the overall stiffness level across aging states.

4. Results and discussions

Acquisition and reconstruction of the experimental 3D microstructure. The initial phase-field microstructure used in this work was obtained from an experimentally reconstructed three-dimensional Ni–CGO anode microstructure reported in [38]. The underlying symmetrical cells were fabricated at Forschungszentrum Jülich GmbH and consisted of an 8YSZ electrolyte with CGO interlayers. The CGO interlayers were prepared from CGO powder, using α-terpineol as dispersion medium and ethylcellulose as transport medium. The NiO/CGO functional layer was prepared analogously from CGO and NiO powders mixed in a 50:50 wt.% ratio. A NiO contact layer was subsequently screen-printed on top of the functional layer and dried overnight at 80 °C. The electrochemical testing and aging treatment were performed at Karlsruhe Institute of Technology. The cells were first heated to 800 °C in nitrogen with a heating rate of 3 $\mathrm{K,min^{-1}}$ and were then reduced stepwise using hydrogen/nitrogen mixtures. After establishing a gas composition corresponding to humidified hydrogen, generated from a hydrogen flow of 0.5 $\mathrm{L,min^{-1}}$ and an oxygen flow of 0.125 $\mathrm{L,min^{-1}}$ in the upstream burner, the resulting H_2/H_2O ratio was 1 : 1. The cells were characterized by electrochemical impedance spectroscopy at 800 °C, 650 °C, and

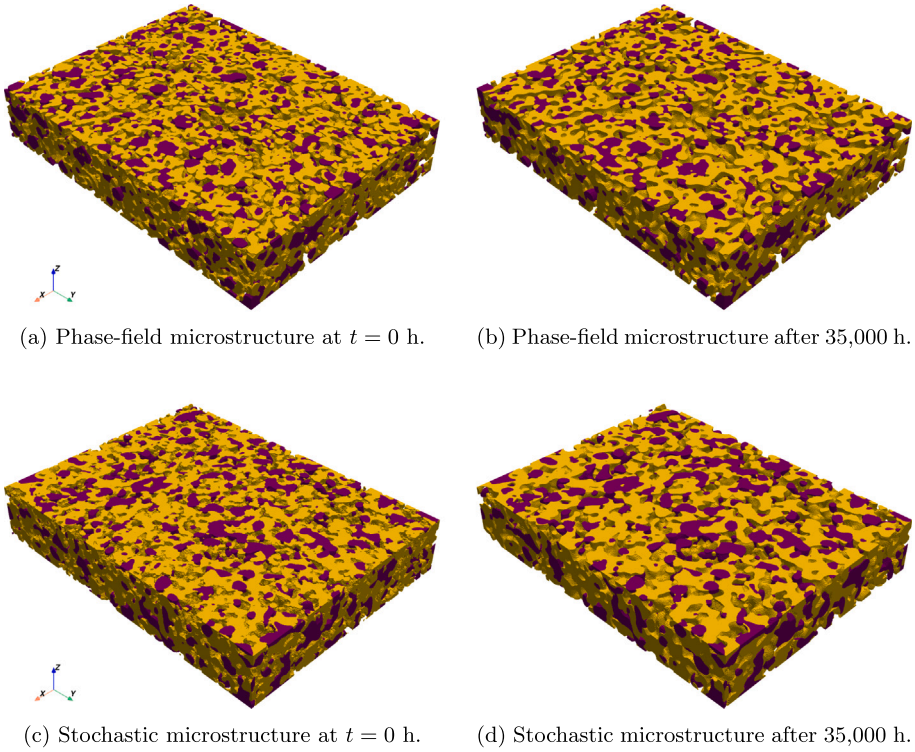

(a) Phase-field microstructure at $t = 0$ h. (b) Phase-field microstructure after 35,000 h.

(c) Stochastic microstructure at $t = 0$ h. (d) Stochastic microstructure after 35,000 h.

Fig. 2. Representative three-dimensional Ni–CGO anode microstructures at the initial state and after 35,000 h of aging. The upper row shows the phase-field microstructure, while the lower row shows a stochastic realization. Ni is shown in purple and CGO in yellow. (For interpretation of the references to colour in this figure legend, the reader is referred to the web version of this article.)

600 °C. Subsequently, the furnace temperature was increased such that the cell temperature reached 900 °C, and the aging experiments were carried out under humidified open-circuit-voltage conditions. Continuous impedance measurements were performed during aging in order to monitor the cell performance while maintaining electrochemical symmetry of the two electrodes. Three cells from the same production batch were considered: one reduced but unaged pristine cell, one cell aged for 240 h, and one cell aged for 1100 h. After operation, the cells were cooled to room temperature in a reducing H_2/N_2 atmosphere with a ratio of $0.05 : 0.95$. The pristine and aged Ni–CGO anode microstructures were reconstructed by FIB–SEM tomography. The pores were first infiltrated with electrically conductive epoxy resin, followed by metallographic sectioning and focused-ion-beam preparation. A Plasma-FIB system was then used to acquire a sequence of SEM images and material slices, resulting in three-dimensional grayscale image stacks. These image stacks were denoised using a Split-Bregman optimization method and segmented by a watershed algorithm. To obtain reliable watershed seeds, threshold values were extracted from the grayscale histogram, and markers close to high-gradient regions and ridge-like features were removed using a Meijering-filter-based procedure. The resulting phase-resolved three-dimensional reconstructions of the pristine, 240 h aged, and 1100 h aged states were used for model initialization and validation in [5].

Microstructures used. For the present analysis, six aged microstructures were considered. These include one aging simulation obtained with the MPFM, as well as five realizations generated by a stochastic reconstruction model to account for statistical variability. The initial phase-field microstructure used in this work was obtained from the experimentally reconstructed three-dimensional Ni-CGO anode microstructure. The phase-field simulation was run to a total aging time of 35,000 h and subsequently employed as input for calibrating the stochastic model parameters. This procedure has been described in detail in Weber et al. [33]. Thus, the phase-field simulation offers a physical basis for understanding microstructural coarsening, whereas the stochastic realizations enhance the statistical assessment of the derived geometric and mechanical descriptors.

Representative three-dimensional microstructures obtained from the phase-field simulation and the stochastic model are shown in Fig. 2 for the initial state and after 35,000 h of aging, with Ni shown in purple and CGO in yellow. The phase-field microstructure was based on the experimentally reconstructed FIB–SEM domain with a voxel size of $\Delta x = \Delta y = \Delta z = 0.05$ μm and physical dimensions of approximately 37.0 μm $\times$ 28.15 μm $\times$ 6.40 μm, corresponding to a total volume of about 6666 μm^3. The stochastic realizations were generated with the same voxel size, domain dimensions and total domain volume. These domains were used as representative volume elements for the calculation of geometrical descriptors and effective mechanical properties.

The following sections present a systematic evaluation of these microstructures in terms of their geometrical characteristics and effective mechanical properties. For brevity, only the geometrical descriptors that are used in the subsequent evaluations in Section 4.3 are presented here.

Remark. The phase-field model used in this work was previously validated against experimentally aged Ni–CGO microstructures up to 1100 h, as reported in [38]. In the present study, the same model is applied to simulate aging up to 35,000 h. This long-term simulation therefore represents an extrapolation beyond the experimentally validated time interval. The extrapolation is based on the assumption that the dominant mechanisms identified within the validated range, namely volume-conserving coarsening driven by surface and interfacial diffusion under isothermal conditions, remain active throughout the considered aging period. The aging duration of 35,000 h was chosen because it is comparable to technologically relevant SOFC operating timescales (e.g., [62]). Direct experimental validation over such durations was not feasible within the scope of the present work. Similar model-based extrapolations to long aging or operating times have been employed in previous SOFC degradation studies [63,64].

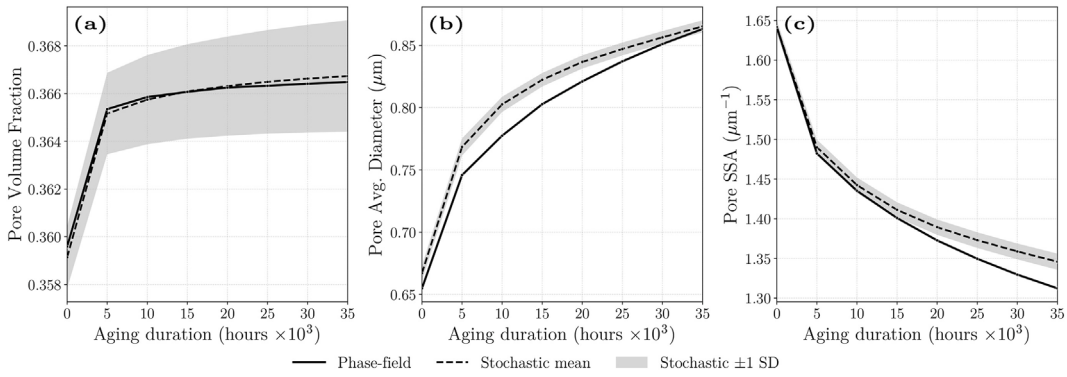

Fig. 3. Evolution of pore microstructural descriptors during aging for phase-field (solid lines) and the five realizations of the stochastic model (dashed lines): (a) volume fraction, (b) mean diameter, and (c) specific surface area. SD: Standard deviation.

4.1. Evolution of selected geometrical descriptors

Pore microstructural properties. Fig. 3 summarizes the evolution of the three key pore descriptors during aging, namely volume fraction, mean diameter, and specific surface area. The pore volume fraction (Fig. 3a) remains within a narrow range throughout the aging process for both methods. In the phase-field simulation, which is calibrated with a free-energy coefficient to preserve phase volumes [35], the porosity stabilizes at approximately 36.6%. The stochastic microstructures exhibit a wider spread across realizations, spanning roughly from 36.4% to 37.0%. While these variations are small in absolute terms, porosity directly reduces the load-bearing cross-section, so even modest differences could contribute to some scatter in the computed effective elastic properties. The porosity variations in the stochastic model remain far below variations encountered in redox cycling scenarios, where Ni oxidation to NiO induces approximately 70% volumetric expansion with severe consequences for mechanical integrity [13].

The mean pore diameter (Fig. 3b) increases monotonically, reflecting the coarsening of the pore network during aging. Both models show very similar values and trend characteristics. The average pore diameter grows from $\approx 0.65\,\mu m$ to approximately $0.86\,\mu m$ over the full aging duration. This coarsening is mirrored by a steady decline in the pore specific surface area (Fig. 3c), which decreases from $1.65\,\mu m^{-1}$ to $1.30 - 1.36\,\mu m^{-1}$. The steepest changes in both quantities occur within the first 5000 hours, after which the coarsening rate progressively diminishes. This decelerating trend is characteristic of diffusion-controlled Ostwald ripening, where the driving force for further coarsening decreases as the curvature differences between particles diminish [65].

Triple phase boundary density. The triple phase boundary density is one of the most critical descriptors for SOFC anodes, as it quantifies the length of lines where the three phases Ni, CGO, and pores coexist and thereby defines the number of electrochemical reaction sites [66]. As has been investigated in the literature [66–68], TPB density shows a pronounced decline during aging, as shown in Fig. 4. In the phase-field simulation, TPB density decreases from an initial value of $2\,\mu m^{-2}$ to about $1.2\,\mu m^{-2}$, corresponding to a reduction of nearly 39%. A similar trend is observed for the stochastic model realizations, where the initial values around $1.9\,\mu m^{-2}$ drop to around $1.08\,\mu m^{-2}$, amounting to a loss of roughly 43%. The predicted TPB degradation is consistent with the limited available long-term experimental observations for Ni–CGO anodes. Zekri et al. [10] investigated porous Ni/CGO anodes after operation times up to 20,000 h using FIB tomography and reported a decrease in TPB density from $3.08\,\mu m^{-2}$ to $1.78\,\mu m^{-2}$, corresponding to a reduction of approximately 42% after 20,000 hours of aging. In their study, the TPB density decreased strongly within the first 2500 h and then continued to decline more gradually up to 20,000 h. This behavior is consistent with the present simulations, where the TPB density decreases most strongly during the early aging period and subsequently approaches a slower long-term degradation rate. This reduction closely mirrors the previously observed increases in mean particle diameter and decreases in SSA. This is consistent with previous considerations from the literature, where an increase in grain size leads to a decrease in the TPB density [69,70]. From a functional perspective, the decline in TPB density directly translates into reduced electrochemical activity and higher polarization resistance [71]. A reduction of 40 – 43% in TPB density implies that nearly half of the active sites vanish during the simulated aging.

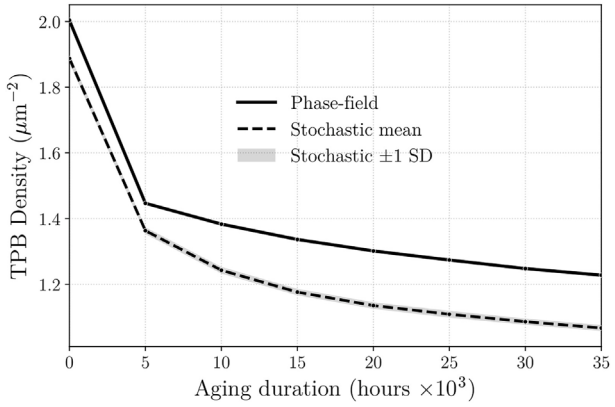

Fig. 4. Evolution of the triple phase boundary density during aging for the phase-field (solid line) and the five realizations of the stochastic model (dashed lines). SD: Standard deviation.

4.2. Effect of aging on effective mechanical properties

Elastic modulus. The boundary conditions and homogenization procedure for the determination of the effective directional elastic moduli and the Hill average are described in detail in Section 3.2.

Fig. 5(a) shows the evolution of the directional elastic moduli for the phase-field microstructure. The initial response is notably anisotropic, where E_{zz} starts at approximately 62.5 GPa, while E_{xx} and E_{yy} begin at around 58 and 57 GPa, respectively. All three directions undergo a steep reduction within the first 5000 hours, after which E_{xx} and E_{yy} stabilize near 55 GPa – 55.5 GPa. The E_{zz} component continues to decrease more gradually, reaching approximately 57 GPa by 35,000 hours. As aging progresses, the three curves show signs of convergence, indicating that the initially anisotropic microstructure becomes increasingly isotropic through grain coarsening. The degree of elastic anisotropy can be quantified by the index $I_A = \max(E_{ii}) - \min(E_{ii})/\langle E_{ii}\rangle$ where $\langle E_{ii}\rangle$ is the average of the three directional elastic moduli. This normalized

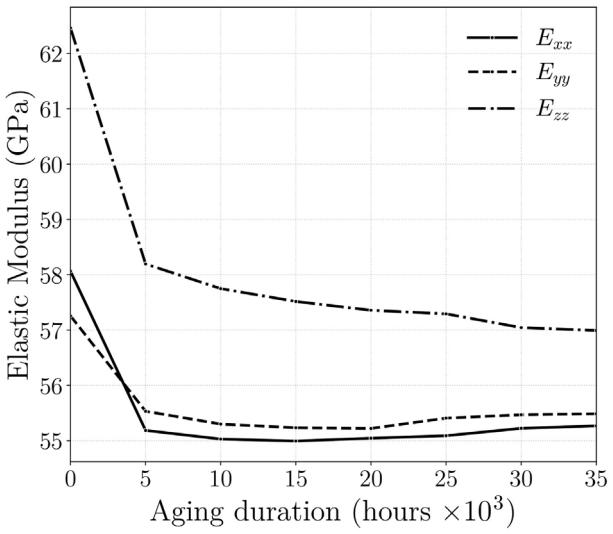

Fig. 5. Evolution of the directional elastic moduli E_{xx}, E_{yy} and E_{zz} during aging for the phase-field microstructure.

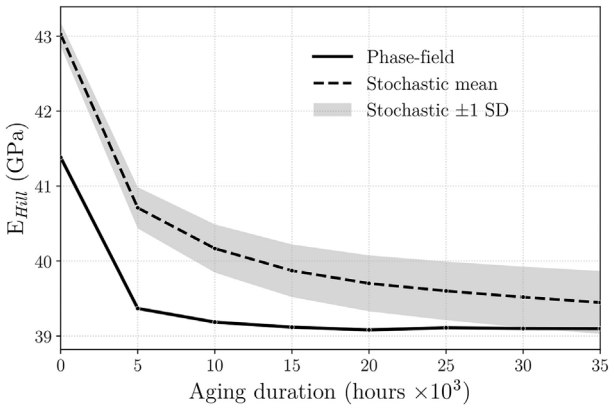

Fig. 6. Evolution of the Hill average elastic modulus during aging for the phase-field (solid line) and the five realizations of the stochastic model (dashed lines). SD: Standard deviation.

measure is used in various contexts to characterize directional stiffness variation, for instance in geological [72], biomedical [73], and fuel cell modeling applications [74]. Consequently, the anisotropy of the initial phase-field microstructure is around 0.09 and decreases to 0.03 after the aging duration. However, it should be noted that the decrease in anisotropy could also be attributed to the isotropic interfacial energy used in this work. Since the initial experimental-based microstructure is anisotropic, the use of anisotropic interfacial energies would be more representative and could lead to a different trend.

The Hill average (Fig. 6) is considered a single scalar measure for the effective elastic modulus and allows a direct comparison between the two modeling approaches. The stochastic realizations start with tightly clustered values around 43 GPa and decrease smoothly to 40 GPa – 39 GPa, corresponding to an average reduction of roughly 7 – 10%. The phase-field microstructure begins at a lower value of approximately 41.5 GPa, drops rapidly to about 39 GPa (∼ 6% decrease) within the first 5000 hours, and then remains nearly constant. Thus, while both approaches capture the general stiffness loss during aging, the stochastic model predicts higher initial elastic modulus and a more gradual degradation, whereas the phase-field simulation exhibits a faster early reduction that saturates sooner. This discrepancy can be attributed to the slight variation in the pore volume fraction, as discussed above, as well as the initial high degree of anisotropy inherent in the experimentally based structure. Such anisotropies are not included in the stochastic model, as discussed in [33]. Nevertheless, as coarsening progresses and the morphological differences between the experimentally derived and stochastically generated structures diminish, the Hill average elastic modulus starts to converge (∼39 GPa – 40 GPa).

Mechanical boundary conditions for realistic operational scenarios. To approximate the mechanical constraints experienced by the anode within a realistic SOFC stack, a boundary condition setup was applied. In this configuration, the anode–electrolyte interface was fixed in all displacement components $(u_x, u_y, u_z) = (0, 0, 0)$, as the anode is anchored to the electrolyte. The opposite surface, corresponding to the anode–interconnect interface, was constrained only in the normal direction ($u_z = 0$), preventing interpenetration with the metallic interconnect. The remaining lateral faces were restricted in displacement normal to their respective planes ($u_n = 0$) mimicking the mechanical confinement imposed by neighboring cells within the stack.

The temperature field was prescribed uniformly as $\theta = 700$ °C throughout the domain, corresponding to an isothermal thermal-loading scenario. With the reference temperature set to $\theta_{\text{ref}} = 25$ °C, the temperature difference in Eq. (15) is therefore $\Delta\theta = \theta - \theta_{\text{ref}} = 675$ K. Unlike the strain-controlled homogenization simulations used to compute the effective elastic moduli (Section 3.2), the stack configuration allows stress and strain fields to evolve naturally under combined mechanical confinement and thermal expansion, providing a more representative basis for assessing stress and strain distributions.

Average von mises stress. The von Mises stress is utilized here as an equivalent scalar measure of the multiaxial stress state, thereby enabling a quantitative comparison of stress levels and their spatial distribution across different microstructures and aging states. It is used solely as an indicator of the overall stress state and is not intended to predict fractures, failure, or damage. The evolution of the average von Mises stress under the applied stack boundary conditions is shown in Fig. 8(a). Here, the average von Mises stress is calculated as $\langle \sigma_{\text{vM}} \rangle = \frac{1}{V} \int_V \sigma_{\text{vM}}(\mathbf{x})\, dV$. Across all datasets, the values vary between 1.15–1.19 GPa (∼ 3.4% difference) throughout the simulated aging period. Hence it can be assumed that the average von Mises stress is essentially constant throughout the 35,000 hours of aging. The absolute values given in this analysis are comparatively high because the simulations assume a purely elastic response without plasticity, creep, or fracture. In reality, stresses above the yield point would relax by inelastic mechanisms. To examine how the von Mises stress is distributed within the microstructure, representative phase-field and stochastic microstructures were selected and their stress probability distributions were evaluated. Fig. 7 shows the corresponding distributions for the initial state (t = 0 h) and after 35,000 h of aging. In both approaches, the stress distributions are concentrated in the low- to intermediate-stress range, whereas very high von Mises stresses occur only with relatively low probability. Overall, the probability decreases with increasing stress level. For the phase-field microstructure, the average von Mises stress increases slightly from 1.160 GPa to 1.177 GPa during aging, and for the stochastic microstructure the average von Mises stress increases slightly from 1.179 GPa to 1.182 GPa. In both approaches, aging is accompanied by a redistribution of the probability percentages. In particular, the aged microstructure exhibits slightly higher probabilities for stresses above 1.5 GPa and, at the same time, for stresses below 0.5 GPa. This suggests that aging does not simply lead to a uniform increase in stress, but rather to a redistribution of stresses within the microstructure. A possible explanation is the smoothing of the microstructure during aging, which reduces the number of thin necks and lowers the stress in some regions, while the remaining thin necks may carry a larger fraction of the load and thus promote local stress concentrations.

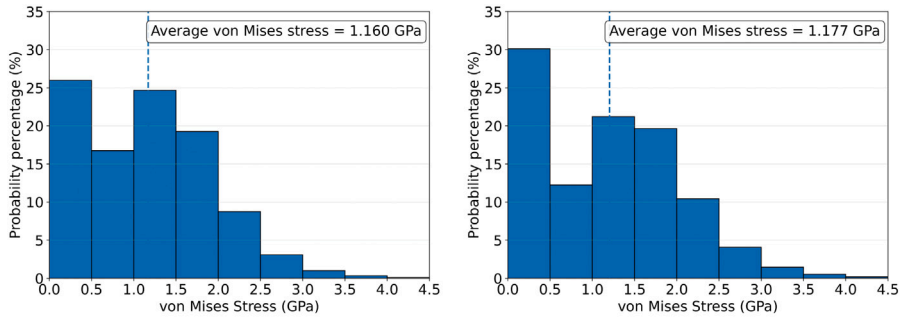

(a) Phase-field microstructure, initial state (b) Phase-field microstructure, aged state

(c) Stochastic microstructure, initial state (d) Stochastic microstructure, aged state

Fig. 7. Probability distributions of the von Mises stress for representative phase-field and stochastic microstructures in the initial and aged states. Panels (a) and (b) show the phase-field microstructure at $t = 0$ h and $t = 35{,}000$ h, respectively, while panels (c) and (d) show a representative stochastic microstructure at the corresponding aging states. The vertical dashed lines indicate the average von Mises stress in each case.

Critical volume fraction. While the average von Mises stress σ_{vm} shows small variation, the fraction of the microstructure experiencing stresses above a critical threshold $\sigma_{threshold}$ increases with aging, as shown in Fig. 8(b). This quantity is here referred to as the critical volume fraction (CVF). It is calculated as

$$\mathrm{CVF} = \frac{1}{V_{\mathrm{tot}}} \int_{V(\sigma_{\mathrm{vM}} > \sigma_{\mathrm{threshold}})} dV. \tag{28}$$

A threshold $\sigma_{threshold}$ =1.19 GPa was chosen for this analysis, as this value corresponds to the upper limit of the average von Mises stress as shown in Fig. 8(a). To assess the sensitivity of the critical volume fraction (CVF) to the selected stress threshold, three threshold values were considered, namely $\sigma_{\mathrm{threshold}}$ = 1.00, 1.19, and 1.50 GPa. The resulting CVF evolution is shown in Fig. B.2 as a function of aging duration. For all three threshold values, the CVF increases with aging for both the phase-field microstructure and the stochastic realizations. The absolute CVF values decrease with increasing threshold, as expected, but the qualitative aging trend remains similar. It should be emphasized that the CVF values are not intended as direct design guidelines or failure criteria. They are used here as comparative indicators of stress redistribution during coarsening, quantifying the fraction of the domain in which the von Mises stress exceeds a prescribed reference threshold. For direct use as a design criterion, the threshold value $\sigma_{\mathrm{threshold}}$ would have to correspond to a physically representative material or failure threshold, such as an appropriate strength value of the anode. Such an interpretation would also require a mechanical model that includes additional mechanisms such as plasticity, creep and fracture. These mechanisms are beyond the scope of the present work.

From a mechanical perspective, the fraction of the microstructure experiencing stresses above a critical threshold provides additional information beyond the average stress level alone. The CVF therefore serves as a measure of how microstructural aging affects the spatial extent of mechanically critical stress states within the microstructure. The CVF rises from about 0.33 initially to 0.37 in the aged state throughout all microstructures. The increasing CVF indicates that aging promotes a redistribution of stress rather than an overall rise in the global stress level (as evident by the nearly constant average von Mises levels). As the microstructure coarsens, some areas become less stressed because local curvatures smooth out or small features disappear, while other areas carry a greater portion of the load. Consequently, even though the overall average von Mises stress stays nearly constant, a larger fraction of the material volume experiences stresses above the critical threshold. This is also reflected in the histograms in Fig. 7. While the average von Mises stress changes very slightly, the aged microstructure shows a redistribution of the probabilities toward stresses above the chosen threshold of 1.19 GPa. This redistribution is consistent with the increase in CVF as a higher fraction of the aged microstructure is exposed to higher stresses compared to the initial microstructure.

4.3. Relating microstructure geometry and mechanical properties

Remark. To better understand how microstructural degradation relates to mechanical performance, pairwise relationships between geometrical descriptors and mechanical properties were analyzed. The considered geometrical descriptors are particle radii, specific surface areas (SSAs), TPB density, and specific pairwise contact areas, while the mechanical quantities include the directional elastic moduli, Hill average elastic modulus, the average von Mises stress, and the critical volume fraction (CVF). For reasons of brevity, only relationships that exhibit clear trends and allow for a consistent physical interpretation are presented below, whereas relationships showing no discernible trend or being dominated by scatter are omitted. Consequently, the following discussion focuses on Hill average elastic modulus and the CVF. The average von Mises stress is not considered further, as it remains nearly constant under the chosen boundary conditions and therefore does not yield meaningful trends with the evolving microstructure.

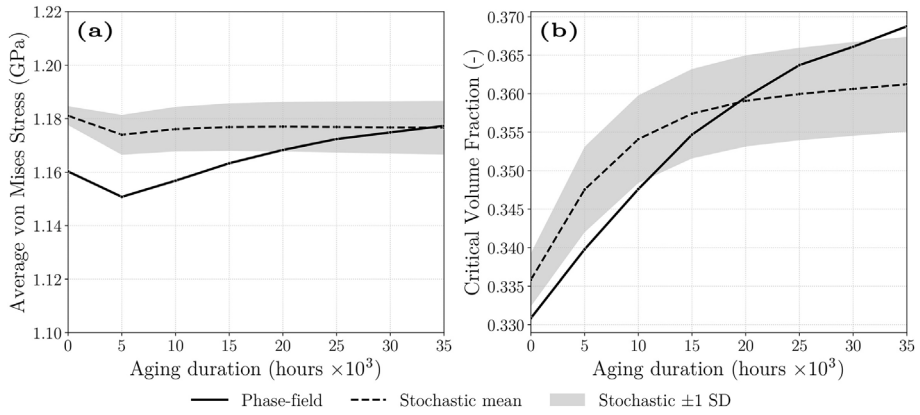

Fig. 8. Evolution of a) the average von Mises stress, and b) the critical volume fraction during aging for the phase-field (solid lines) and the five realizations of the stochastic model (dashed lines). SD: Standard deviation.

As the objective of this section is to identify general relationships rather than method-specific differences, no distinction is made between phase-field and stochastic microstructures. Instead, all data points are treated as a single pooled dataset. The relationships shown below were quantified by least-squares regression. Depending on the observed trend, either a linear regression or a second-degree polynomial regression was applied. The deviations reported below correspond to the maximum positive and negative relative deviations from the fitted curve and are defined (in %) as

$$\delta_i = 100 \times \frac{y_i - \hat{y}_i}{\hat{y}_i}, \tag{29}$$

where y_i denotes the computed value and $\hat{y}_i$ the corresponding value predicted by the regression model. The limitations of this analysis should however be emphasized. The descriptor–property relationships presented here are descriptive trends derived from the investigated phase-field and stochastic aging trajectories. The data points therefore represent microstructures generated from the present model assumptions and within the limited composition and particle sizes considered in this work. Accordingly, the observed trends should be interpreted as microstructure–property associations for the present dataset, rather than as generalizable correlations for arbitrary Ni–CGO anode microstructures. Assessing their generalizability requires systematic variations of phase volume fractions and particle-size distributions, which is beyond the scope of the present work.

Elastic modulus. Establishing a relation between the Hill average elastic modulus E_{Hill} and the microstructural descriptors provides a direct link between mechanical stiffness and geometric coarsening. Fig. 9 shows that E_{Hill} decreases approximately linearly with increasing pore volume fraction. While the pore fraction variations observed during aging are relatively small (around 1.5% across all data, cf. Section 4.1), these modest changes are already associated with measurable reductions in E_{Hill}. This is consistent with other homogenization schemes (e.g., Voigt homogenization), according to which the phase volume fractions contribute directly to the effective elastic response. The relationship is consistent across datasets, with relative deviations δ_i within -1.9% and $+$ 3.3%. This sensitivity reflects the strong role of porosity in reducing the effective load-bearing cross-section, consistent with previous studies on porous SOFC anodes [13,23].

Additionally, the Hill average modulus increases with the specific surface area of the pore phase. Within the microstructures investigated, this relationship is well captured by a second-degree polynomial fit, with δ_i between -3.2% and $+$ 1.8%. A higher pore SSA corresponds to a finer, more distributed pore network, whereas a lower SSA indicates that the pore space has coarsened into fewer, larger voids. As pores coarsen, the surrounding solid phases lose interfacial contact area and local load-transfer paths are disrupted. Conversely, a finer pore morphology preserves a more continuous and well-connected solid skeleton. The pore SSA thus serves as an indirect measure of the connectivity of the Ni–CGO network. Its decrease during aging reflects not only pore coarsening itself, but also the accompanying degradation of the solid-phase connectivity. Even though the Ni volume fraction remains nearly constant, the (distinct) decrease in the effective Young's modulus is attributed to the increase in the pore volume fraction.

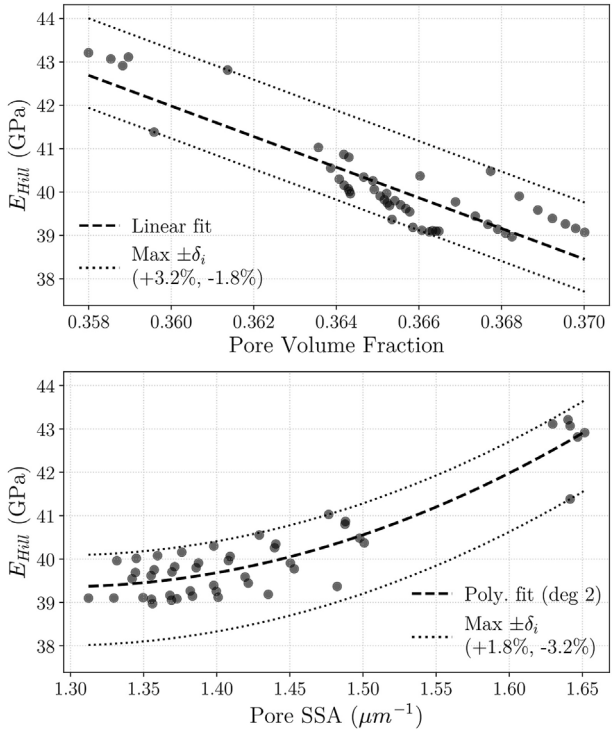

Fig. 9. Relationship between the Hill average elastic modulus (E_{Hill}) and the pore phase volume fraction (top), and the specific surface area of the pore phase (bottom).

Critical volume fraction. In the microstructures under investigation, the critical volume fraction—representing the volume fraction exceeding a von Mises stress of 1.19 GPa—exhibits a strong dependence on the geometric characteristics of the pore phase, as well as on the TPB density. As shown in Fig. 10 (top and middle rows), CVF increases

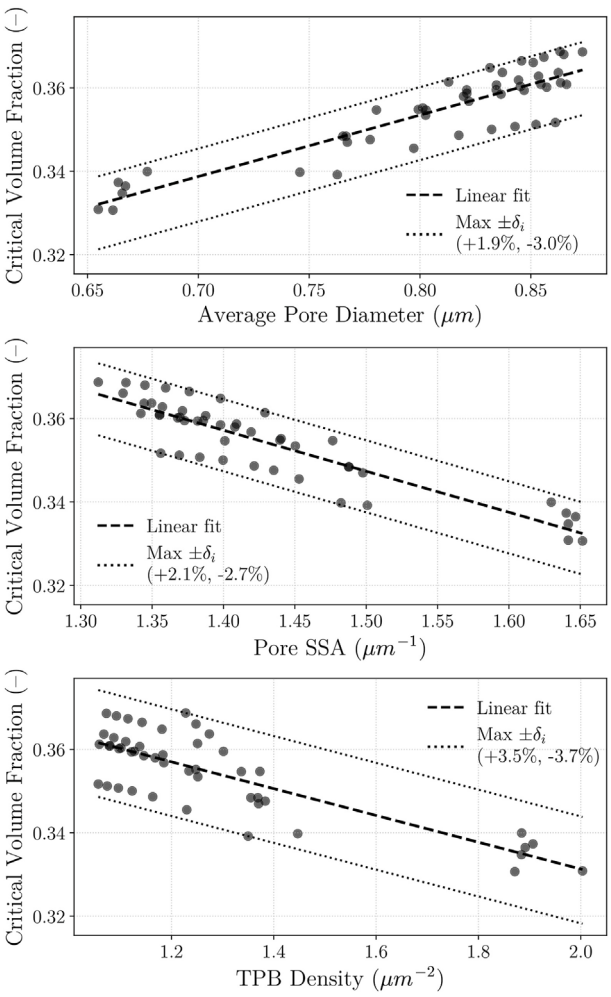

Fig. 10. Relationship between the critical volume fraction and the average pore diameter (top), the specific surface area of the pore phase (middle) and the triple phase boundary density (bottom).

nearly linearly with the mean pore diameter, while it decreases correspondingly with SSA of the pore phase. The mean pore diameter exhibits a clear relationship with the CVF across all simulations, with relative deviations δ_i between -3.0% and $+$ 1.9%. The SSA of the pore phase shows a similar but opposite trend, with δ_i ranging from -2.7% to $+$ 2.1%. Consequently, these opposing trends are manifestations of the morphological transformation due to pore coarsening. Furthermore, a negative relationship is observed between the CVF and the TPB density, with relative deviations δ_i between -3.7% and $+$ 3.5% across all datasets (Fig. 10, bottom row). This suggests that, for the present aging trajectories, the reduction in TPB density during coarsening coincides with a redistribution of the stress field toward a larger volume fraction exceeding the prescribed threshold. From a mechanical perspective, TPB density acts as a quantitative descriptor of microstructural fineness and phase interpenetration. As the TPB network deteriorates through coarsening and interface loss, the critical volume fraction increases.

5. Concluding remarks

This work presented a fully automated and FAIR-compliant workflow for analyzing the morphological and mechanical evolution of Ni–CGO anodes, implemented in KadiStudio within the Kadi4Mat infrastructure [28]. The workflow imports microstructures locally or from the Kadi4Mat repository, runs mechanical simulations, and computes the geometrical descriptors as well as the effective mechanical properties of the microstructure. The results and metadata are uploaded to the Kadi4Mat repository for reproducibility. One microstructure reconstructed from real Ni-CGO anode image data aged up to 35,000 hours [5] using the multiphase-field method and five realizations of the stochastic model outlined in [33] were investigated. The geometrical analysis revealed that phase fractions remain essentially constant during aging, confirming that degradation is driven primarily by interface reduction rather than bulk volume change. Coarsening manifests as an increase in the mean particle diameter and a decrease in specific surface area and triple phase boundary density. Numerical homogenization revealed a reduction in the effective stiffness, quantified through the directional elastic modulus and the Hill average modulus. This reduction in stiffness was consistent across all datasets and showed a clear relationship with the specific surface area of the pore phase, highlighting that microstructural fineness and pore network connectivity play a role in the effective mechanical behavior within the investigated microstructures. Under the stack boundary conditions representing anode confinement within the SOFC assembly, the spatial stress distribution, arising due to thermal expansion, displayed distinct behavior, where the average von Mises stress remained nearly constant due to the macroscopic boundary constraints, while the volume fraction exceeding a critical stress threshold increased with time. This increase in critical volume fraction reflects a stress redistribution, as a higher fraction of the microstructure experiences higher stresses. In the set of microstructures studied, the critical volume fraction was found to be positively related to the average pore diameter, and negatively related to triple phase boundary density and specific surface area of the pore phase. Thus, the critical volume fraction directly links microstructural degradation to mechanical weakening and simultaneously connects electrochemical and mechanical descriptors. These results demonstrate that microstructural coarsening in Ni–CGO anodes not only reduces electrochemically active interfaces (degrading electrochemical performance) but also degrades effective mechanical properties of the anode at the investigated composition and particle sizes. Overall, the findings and microstructure–property relationships establish a basis for advancing electrode material optimization by enabling the comparison of microstructures. The mechanical properties predicted in this work should be interpreted as comparative microstructure-level descriptors under the considered isothermal coarsening scenario, rather than as direct design allowables for arbitrary SOFC operating conditions. In this sense, the effective elastic moduli, von Mises stresses, and critical volume fractions can support electrode optimization by identifying stiffness changes and stress-localization tendencies associated with evolving Ni–CGO–pore morphologies. Direct transfer to electrode design and manufacture, however, requires further investigations over a broader microstructural parameter space, including systematic variations of phase volume fractions [64] and particle-size distributions. Recent model-based and digital-electrode studies further highlight the potential of simulation-assisted microstructure optimization for SOFC electrodes [75–78]. The established workflow provides a suitable basis for such extended analyses, since it enables coupled geometrical and mechanical evaluations to be performed automatically and reproducibly, with results and metadata stored in Kadi4Mat for future reuse.

CRediT authorship contribution statement

Ahmed Elmoghazy: Writing – original draft, Visualization, Software, Methodology, Conceptualization, Writing – review & editing. **Sabrina Weber:** Writing – review & editing, Software, Methodology, Data curation, Writing – original draft. **Ravi Kumar Jeela:** Writing – review & editing, Data curation. **Andreas Prahs:** Writing – review & editing, Supervision, Methodology, Conceptualization. **Benedikt Prifling:** Writing – review & editing, Supervision, Methodology, Conceptualization. **Daniel Schneider:** Writing – review & editing, Supervision, Methodology, Conceptualization. **Volker Schmidt:** Writing

– review & editing, Supervision, Resources, Project administration, Funding acquisition, Conceptualization. **Britta Nestler:** Writing – review & editing, Supervision, Resources, Project administration, Funding acquisition, Conceptualization.

Declaration of Generative AI and AI-assisted technologies in the writing process

During the preparation of this work the author used ChatGPT 5.4 to assist with language editing and improve readability. After using this tool, the author reviewed and edited the content as needed and takes full responsibility for the content of the published article.

Declaration of competing interest

The authors declare the following financial interests/personal relationships which may be considered as potential competing interests:

Britta Nestler reports that financial support was provided by Federal Ministry of Research, Technology and Space of Germany. If there are other authors, they declare that they have no known competing financial interests or personal relationships that could have appeared to influence the work reported in this paper.

Acknowledgements

The authors would like to thank the Federal Ministry of Research, Technology and Space (BMFTR) for financial support within the priority program “Mathematics for Innovations” in the framework of “DASEA-4-SOFC” (grant number 05M2022). The financial support of the MTET program (no. 38.02.01) of Helmholtz Association is gratefully acknowledged. The authors acknowledge support by the state of Baden-Württemberg through bwHPC.

Appendix A. Workflow in KadiStudio

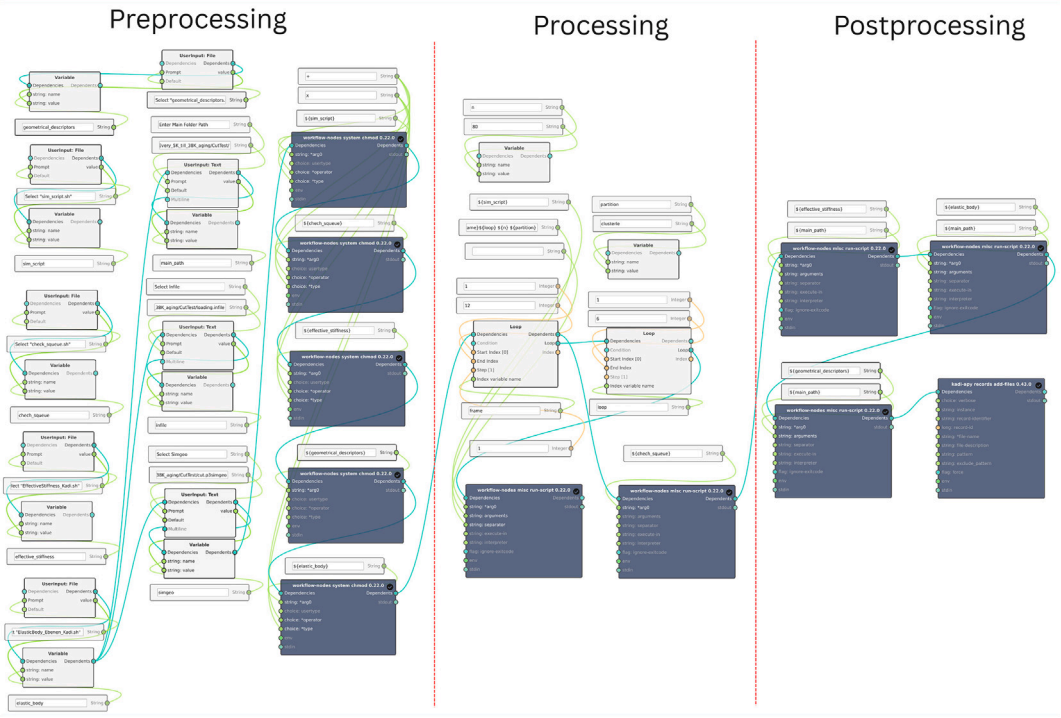

Fig. A.1. A screenshot from KadiStudio showing the implemented workflow.

Appendix B. Sensitivity analysis of the CVF with respect to the chosen threshold stress

To assess the sensitivity of the critical volume fraction (CVF) to the selected stress threshold, three threshold values were considered: $\sigma_{\text{threshold}} = 1.00$, 1.19, and 1.50 GPa (Fig. B.2). For $\sigma_{\text{threshold}} = 1.00$ GPa, the phase-field CVF increases from approximately 0.426 in the initial state to 0.455 after 35,000 h of aging, while the stochastic mean increases from about 0.433 to 0.447. For the threshold used in the main analysis, $\sigma_{\text{threshold}} = 1.19$ GPa, the corresponding values increase from approximately 0.331 to 0.369 for the phase-field microstructure and from about 0.336 to 0.361 for the stochastic mean. For the highest threshold, $\sigma_{\text{threshold}} = 1.50$ GPa, the CVF values are lower, increasing from approximately 0.197 to 0.236 for the phase-field microstructure and from about 0.201 to 0.232 for the stochastic mean. Thus, increasing the threshold reduces the absolute CVF values, as expected, because a smaller fraction of the microstructure exceeds a higher stress level. However, the qualitative aging trend remains consistent for all three thresholds.

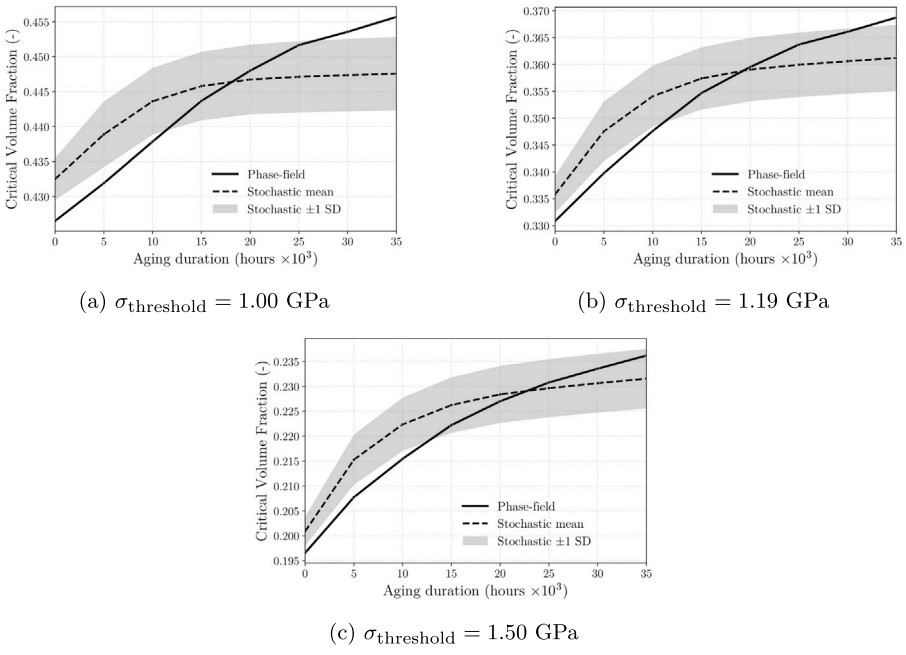

(a) $\sigma_{\text{threshold}} = 1.00$ GPa (b) $\sigma_{\text{threshold}} = 1.19$ GPa

(c) $\sigma_{\text{threshold}} = 1.50$ GPa

Fig. B.2. Sensitivity of the critical volume fraction (CVF) to the selected stress threshold.

Data availability

The data are available from the authors upon reasonable request.

References

[1] S. Vafaeenezhad, A.R. Hanifi, M.A. Laguna-Bercero, T.H. Etsell, P. Sarkar, Microstructure and long-term stability of Ni–YSZ anode supported fuel cells: a review, Mater. Futures 1 (4) (2022) 042101, https://doi.org/10.1088/2752-5724/ac88e7

[2] Y. Liu, M. Juckel, N.H. Menzler, A. Weber, Ni/GDC fuel electrode for low-temperature SOFC and its aging behavior under accelerated stress, J. Electrochem. Soc. 171 (5) (2024) 054514, https://doi.org/10.1149/1945-7111/ad4917

[3] P. Vinchhi, M. Khandla, K. Chaudhary, R. Pati, Recent advances on electrolyte materials for SOFC: a review, Inorg. Chem. Commun. 152 (2023) 110724, https://doi.org/10.1016/j.inoche.2023.110724

[4] A. Nenning, C. Bischof, J. Fleig, M. Bram, A.K. Opitz, The relation of microstructure, materials properties and impedance of SOFC electrodes: a case study of Ni/GDC anodes, Energies 13 (4) (2020) 987, https://doi.org/10.3390/en13040987

[5] R.K. Jeela, G. Tosato, M. Ahmad, M. Wieler, A. Koeppe, B. Nestler, et al., Enhancing solid oxide fuel cells development through Bayesian active learning, Adv. Energy Mater. 15 (34) (2025), https://doi.org/10.1002/aenm.202501216

[6] J. Peng, D. Zhao, Y. Xu, X. Wu, X. Li, Comprehensive analysis of solid oxide fuel cell performance degradation mechanism, prediction, and optimization studies, Energies 16 (2) (2023) 788, https://doi.org/10.3390/en16020788

[7] X. Yang, Z. Du, Q. Zhang, Z. Lyu, S. Liu, Z. Liu, et al., Effects of operating conditions on the performance degradation and anode microstructure evolution of anode-supported solid oxide fuel cells, Int. J. Miner. Metall. Mater. 30 (6) (2023) 1181–1189, https://doi.org/10.1007/s12613-023-2616-7

[8] F.R. Bianchi, A.K. Padinjarethil, A. Hagen, B. Bosio, Multiscale analysis of Ni-YSZ and Ni-CGO anode based SOFC degradation: from local microstructural variation to cell electrochemical performance, Electrochim. Acta 460 (2023) 142589, https://doi.org/10.1016/j.electacta.2023.142589

[9] A. Sciazko, T. Shimura, Y. Komatsu, N. Shikazono, Ni-GDC and Ni-YSZ electrodes operated in solid oxide electrolysis and fuel cell modes, J. Therm. Sci. Technol. 16 (1) (2021) JTST0013, https://doi.org/10.1299/jtst.2021jtst0013

[10] A. Zekri, M. Knipper, J. Parisi, T. Plaggenborg, Microstructure degradation of Ni/CGO anodes for solid oxide fuel cells after long operation time using 3D reconstructions by FIB tomography, Phys. Chem. Chem. Phys. 19 (21) (2017) 13767–13777, https://doi.org/10.1039/c7cp02186k

[11] T. Klemensø, M. Mogensen, Ni–YSZ solid oxide fuel cell anode behavior upon redox cycling based on electrical characterization, J. Am. Ceram. Soc. 90 (11) (2007) 3582–3588, https://doi.org/10.1111/j.1551-2916.2007.01909.x

[12] A. Faes, A. Nakajo, A. Hessler-Wyser, D. Dubois, A. Brisse, S. Modena, et al., RedOx study of anode-supported solid oxide fuel cell, J. Power Sources 193 (1) (2009) 55–64, https://doi.org/10.1016/j.jpowsour.2008.12.118

[13] B. Song, E. Ruiz-Trejo, A. Bertei, N.P. Brandon, Quantification of the degradation of Ni-YSZ anodes upon redox cycling, J. Power Sources 374 (2018) 61–68, https://doi.org/10.1016/j.jpowsour.2017.11.024

[14] M. Ettler, H. Timmermann, J. Malzbender, A. Weber, N.H. Menzler, Durability of ni anodes during reoxidation cycles, J. Power Sources 195 (17) (2010) 5452–5467, https://doi.org/10.1016/j.jpowsour.2010.03.049

[15] R. Basu, S.S. Kumar, A.K. Mukhopadhyay, H.S. Maiti, Improvement in mechanical properties of anode-supported planar SOFC, ECS Trans. 7 (1) (2007) 533–541, https://doi.org/10.1149/1.2729133

[16] S. Zhou, Y. Zeng, X. Liu, X. Li, C.L. Martin, N. Shikazono, et al., Accessing elastic properties of porous solid oxide fuel cell electrodes using 2D image-based discrete element modeling and deep learning, Acta Mech. Solida Sin. 38 (3) (2024) 384–401, https://doi.org/10.1007/s10338-024-00535-y

[17] B.R. Roy, N.M. Sammes, T. Suzuki, Y. Funahashi, M. Awano, Mechanical properties of micro-tubular solid oxide fuel cell anodes, J. Power Sources 188 (1) (2009) 220–224, https://doi.org/10.1016/j.jpowsour.2008.11.076

[18] A. Masini, T. Strohbach, F. Šiška, Z. Chlup, I. Dlouhý, Electrolyte-supported fuel cell: co-sintering effects of layer deposition on biaxial strength, Materials 12 (2) (2019) 306, https://doi.org/10.3390/ma12020306

[19] M. Morales, M.A. Laguna-Bercero, E. Jiménez-Piqué, Direct-methane anode-supported solid oxide fuel cells fabricated by aqueous gel-casting, J. Eur. Ceram. Soc. 43 (7) (2023) 2740–2751, https://doi.org/10.1016/j.jeurceramsoc.2022.06.027

[20] T.M.M. Heenan, J.B. Robinson, X. Lu, B. Tjaden, A. Cervellino, J.J. Bailey, et al., Understanding the thermo-mechanical behaviour of solid oxide fuel cell anodes using synchrotron X-ray diffraction, Solid State Ion. 314 (2018) 156–164, https://doi.org/10.1016/j.ssi.2017.10.025

[21] J.H. Park, J.H. Lee, K.J. Yoon, H. Kim, H.I. Ji, S. Yang, et al., A nanoarchitectured cermet composite with extremely low ni content for stable high-performance solid oxide fuel cells, Acta Mater. 206 (2021) 116580, https://doi.org/10.1016/j.actamat.2020.116580

[22] L.J. Gibson, M.F. Ashby, Cellular Solids: Structure and Properties, Cambridge University Press, 1997.

[23] M. Pihlatie, A. Kaiser, M. Mogensen, Mechanical properties of NiO/Ni–YSZ composites depending on temperature, porosity and redox cycling, J. Eur. Ceram. Soc. 29 (9) (2009) 1657–1664, https://doi.org/10.1016/j.jeurceramsoc.2008.10.017

[24] W. Pabst, E. Gregorová, G. Tichá, Elasticity of porous ceramics - a critical study of modulus porosity relations, J. Eur. Ceram. Soc. 26 (7) (2006) 1085–1097, https://doi.org/10.1016/j.jeurceramsoc.2005.01.041

[25] Z. Chen, X. Wang, F. Giuliani, A. Atkinson, Analyses of microstructural and elastic properties of porous SOFC cathodes based on focused ion beam tomography, J. Power Sources 273 (2015) 486–494, https://doi.org/10.1016/j.jpowsour.2014.09.131

[26] L. Liu, G.Y. Kim, A. Chandra, Modeling of Ni–CGO anode in a solid oxide fuel cell deposited by spray pyrolysis, J. Power Sources 210 (2012) 129–137, https://doi.org/10.1016/j.jpowsour.2012.03.031

[27] X. Lu, T.M.M. Heenan, J.J. Bailey, T. Li, K. Li, D.J.L. Brett, et al., Correlation between triple phase boundary and the microstructure of solid oxide fuel cell anodes: the role of composition, porosity and ni densification, J. Power Sources 365 (2017) 210–219, https://doi.org/10.1016/j.jpowsour.2017.08.095

[28] N. Brandt, L. Griem, C. Herrmann, E. Schoof, G. Tosato, Y. Zhao, et al., Kadi4Mat: a research data infrastructure for materials science, Data Sci. J. 20 (2021) 8, https://doi.org/10.5334/dsj-2021-008

[29] L. Griem, P. Zschumme, M. Laqua, N. Brandt, E. Schoof, P. Altschuh, et al., KadiStudio: FAIR modelling of scientific research processes, Data Sci. J. 21 (2022), https://doi.org/10.5334/dsj-2022-016
[30] I. Steinbach, F. Pezzolla, A generalized field method for multiphase transformations using interface fields, Phys. D Nonlinear Phenom. 134 (4) (1999) 385–393, https://doi.org/10.1016/S0167-2789(99)00129-3
[31] B. Nestler, A. Choudhury, Phase-field modeling of multi-component systems, Curr. Opin. Solid State Mater. Sci. 15 (3) (2011) 93–105, https://doi.org/10.1016/j.cossms.2011.01.003
[32] A. Prahs, D. Schneider, B. Nestler, A continuum thermodynamic approach to the phase-field method: the order parameter as internal state variable, Contin. Mech. Thermodyn. 37 (4) (2025) 55, https://doi.org/10.1007/s00161-025-01383-y
[33] S. Weber, B. Prifling, R.K. Jeela, A. Prahs, D. Schneider, B. Nestler, et al., A time-continuous approach to analyzing anode aging in solid-oxide fuel cells via stochastic 3D microstructure modeling and physics-based simulations, Comput. Mater. Sci. 264 (2026) 114491, https://doi.org/10.1016/j.commatsci.2026.114491
[34] A. Choudhury, B. Nestler, Grand-potential formulation for multicomponent phase transformations combined with thin-interface asymptotics of the double-obstacle potential, Phys. Rev. E 85 (2) (2012) 021602, https://doi.org/10.1103/PhysRevE.85.021602
[35] P.W. Hoffrogge, A. Mukherjee, E.S. Nani, P.G.K. Amos, F. Wang, D. Schneider, et al., Multiphase-field model for surface diffusion and attachment kinetics in the grand-potential framework, Phys. Rev. E 103 (3) (2021) 033307, https://doi.org/10.1103/PhysRevE.103.033307
[36] B. Nestler, H. Garcke, B. Stinner, Multicomponent alloy solidification: phase-field modeling and simulations, Phys. Rev. E 71 (4) (2005) 041609, https://doi.org/10.1103/PhysRevE.71.041609
[37] M. Seiz, P. Hoffrogge, H. Hierl, A. Reiter, D. Schneider, B. Nestler, Phase-field simulations with the grand potential approach, in: High Performance Computing in Science and Engineering '20, Springer International Publishing, 2021, pp. 561–577.
[38] R.K. Jeela, M. Ahmad, M. Wieler, Y. Liu, M. Juckel, D. Schneider, et al., Multiphase-field simulation studies of coarsening in Ni-GDC SOFC anode microstructures and the effect of interfacial energies, ACS Appl. Energy Mater. 8 (24) (2025) 17670–17687, https://doi.org/10.1021/acsaem.5c02218
[39] A. Semenov, E. Langner, M. El Hachemi, S. Belouettar, T. Wallmersperger, Modelling and simulation of the electro-chemo-thermo-mechanical behaviour of solid oxide fuel cells considering creep, Acta Mech. (2025), https://doi.org/10.1007/s00707-025-04334-5
[40] D. Schneider, O. Tschukin, A. Choudhury, M. Selzer, T. Böhlke, B. Nestler, Phase-field elasticity model based on mechanical jump conditions, Comput. Mech. 55 (5) (2015) 887–901, https://doi.org/10.1007/s00466-015-1141-6
[41] A. Durga, P. Wollants, N. Moelans, Evaluation of interfacial excess contributions in different phase-field models for elastically inhomogeneous systems, Model. Simul. Mater. Sci. Eng. 21 (5) (2013) 055018, https://doi.org/10.1088/0965-0393/21/5/055018
[42] J. Mosler, O. Shchyglo, H. Montazer Hojjat, A novel homogenization method for phase field approaches based on partial rank-one relaxation, J. Mech. Phys. Solids 68 (2014) 251–266, https://doi.org/10.1016/j.jmps.2014.04.002
[43] D. Schneider, F. Schwab, E. Schoof, A. Reiter, C. Herrmann, M. Selzer, et al., On the stress calculation within phase-field approaches: a model for finite deformations, Comput. Mech. 60 (2) (2017) 203–217, https://doi.org/10.1007/s00466-017-1401-8
[44] R. Farraro, R.B. Mclellan, Temperature dependence of the young's modulus and shear modulus of pure nickel, platinum, and molybdenum, Metall. Trans. A 8 (10) (1977) 1563–1565, https://doi.org/10.1007/bf02644859
[45] P. Hidnert, Thermal expansion of some nickel alloys, J. Res. Natl. Bur. Stand. 58 (2) (1957) 89–92.
[46] X. Fan, E.D. Case, Q. Yang, J.D. Nicholas, Room temperature elastic properties of gadolinia-doped ceria as a function of porosity, Ceram. Int. 39 (6) (2013) 6877–6886, https://doi.org/10.1016/j.ceramint.2013.02.022
[47] K.B. Andersen, B. Charlas, E. Stamate, K.K. Hansen, Permeability, strength and electrochemical studies on ceramic multilayers for solid-state electrochemical cells, Heliyon 3 (8) (2017) e00371, https://doi.org/10.1016/j.heliyon.2017.e00371
[48] C. Lantuéjoul, Geostatistical Simulation: Models and Algorithms, Springer, 2013.
[49] S.N. Chiu, D. Stoyan, W.S. Kendall, J. Mecke ed), Stochastic Geometry and Its Applications, third ed, John Wiley & Sons, 2013.
[50] I. Molchanov, Theory of Random Sets, Springer, 2005.
[51] C. Draxl, M. Scheffler, Big data-driven materials science and its FAIR data infrastructure, in: Handbook of Materials Modeling, Springer International Publishing, 2020, pp. 49–73.
[52] J. Hötzer, A. Reiter, H. Hierl, P. Steinmetz, M. Selzer, B. Nestler, The parallel multi-physics phase-field framework Pace3D, J. Comput. Sci. 26 (2018) 1–12, https://doi.org/10.1016/j.jocs.2018.02.011
[53] B. Münch, L. Holzer, Contradicting geometrical concepts in pore size analysis attained with electron microscopy and mercury intrusion, J. Am. Ceram. Soc. 91 (12) (2008) 4059–4067, https://doi.org/10.1111/j.1551-2916.2008.02736.x
[54] L. Holzer, B. Iwanschitz, T. Hocker, B. Münch, M. Prestat, D. Wiedenmann, et al., Microstructure degradation of cermet anodes for solid oxide fuel cells: quantification of nickel grain growth in dry and in humid atmospheres, J. Power Sources 196 (3) (2011) 1279–1294, https://doi.org/10.1016/j.jpowsour.2010.08.017
[55] K. Palàgyi, A. Kuba, A 3D 6-subiteration thinning algorithm for extracting medial lines, Pattern Recognit. Lett. 19 (7) (1998) 613–627, https://doi.org/10.1016/s0167-8655(98)00031-2
[56] P.W. Hoffrogge, D. Schneider, F. Wankmüller, M. Meffert, D. Gerthsen, A. Weber, et al., Performance estimation by multiphase-field simulations and transmission-line modeling of nickel coarsening in FIB-SEM reconstructed Ni-YSZ SOFC anodes I: influence of wetting angle, J. Power Sources 570 (2023) 233031, https://doi.org/10.1016/j.jpowsour.2023.233031
[57] L. Kehrer, P. Pinter, T. Böhlke, Mean and full field homogenization of artificial long fiber reinforced thermoset polymers, PAMM 17 (1) (2017) 603–604, https://doi.org/10.1002/pamm.201710271
[58] A. Bertram, R. Glüge, Solid Mechanics: Theory, Modeling, and Problems, Springer International Publishing, 2015.
[59] A. Bertram, Elasticity and Plasticity of Large Deformations: Including Gradient Materials, Springer International Publishing, 2021.
[60] T. Böhlke, C. Brüggemann, Graphical representation of the generalized hooke's law, Tech. Mech. -Eur. J. Eng. Mech. 21 (2) (2019) 145–158.
[61] R. Hill, The elastic behaviour of a crystalline aggregate, Proc. Phys. Soc. A 65 (5) (1952) 349–354, https://doi.org/10.1088/0370-1298/65/5/307
[62] L. Blum, Q. Fang, S.M. Groß-Barsnick, L.G.J.B. de Haart, J. Malzbender, N.H. Menzler, et al., Long-term operation of solid oxide fuel cells and preliminary findings on accelerated testing, Int. J. Hydrog. Energy 45 (15) (2020) 8955–8964, https://doi.org/10.1016/j.ijhydene.2020.01.074
[63] J. Mason, I. Celik, S. Lee, H. Abernathy, G. Hackett, Performance degradation predictions based on microstructural evolution due to grain coarsening effects in solid oxide fuel cell electrodes, J. Electrochem. Soc. 165 (2) (2018) F64–F74, https://doi.org/10.1149/2.0721802jes
[64] R.K. Jeela, A. Elmoghazy, L. Schöller, M. Wieler, A. Prahs, D. Schneider, et al., Effect of volume fractions and aging on Ni-GDC SOFC anode degradation and performance: multiphase-field simulations, NPJ Mater. Degrad. (2026), https://doi.org/10.1038/s41529-026-00811-x
[65] W. Mullins, Grain boundary grooving by volume diffusion, Trans. Am. Inst. Min. Metall. Eng. 218 (2) (1960) 354–361.
[66] B. Kenney, M. Valdmanis, C. Baker, J.G. Pharoah, K. Karan, Computation of TPB length, surface area and pore size from numerical reconstruction of composite solid oxide fuel cell electrodes, J. Power Sources 189 (2) (2009) 1051–1059, https://doi.org/10.1016/j.jpowsour.2008.12.145
[67] M. Nerat, A model of solid oxide fuel cell degradation on a microstructural level, Appl. Sci. 10 (6) (2020) 1906, https://doi.org/10.3390/app10061906
[68] P.W. Hoffrogge, S. Daubner, D. Schneider, B. Nestler, B. Zhou, J. Eiken, Triple junction benchmark for multiphase-field models combining capillary and bulk driving forces, Model. Simul. Mater. Sci. Eng. 33 (1) (2024) 015001, https://doi.org/10.1088/1361-651x/ad8d6f
[69] X. Deng, A. Petric, Geometrical modeling of the triple-phase-boundary in solid oxide fuel cells, J. Power Sources 140 (2) (2005) 297–303, https://doi.org/10.1016/j.jpowsour.2004.08.046
[70] B. Timurkutluk, Y. Ciflik, T. Altan, O. Genc, Synthetical designing of solid oxide fuel cell electrodes: effect of particle size and volume fraction, Int. J. Hydrog. Energy 47 (73) (2022) 31446–31458, https://doi.org/10.1016/j.ijhydene.2022.07.071
[71] E.C. Miller, Q. Sherman, Z. Gao, P.W. Voorhees, S.A. Barnett, Stability of nickel-infiltrated anodes in intermediate temperature SOFCs, ECS Trans. 68 (1) (2015) 1245–1254, https://doi.org/10.1149/06801.1245ecst
[72] K.E. Noble Tsidzi, The influence of foliation on point load strength anisotropy of foliated rocks, Eng. Geol. 29 (1) (1990) 49–58, https://doi.org/10.1016/0013-7952(90)90081-b
[73] X.H. Cheng, H.M. Chen, Q. Chen, Anisotropic characterization of different materialized scaffolds: a numerical study, Biomed. Eng. Commun. 2 (2) (2023) 12, https://doi.org/10.53388/bmec2023012
[74] S.A. Tabei, A. Sheidaei, M. Baniassadi, F. Pourboghrat, H. Garmestani, Microstructure reconstruction and homogenization of porous Ni-YSZ composites for temperature dependent properties, J. Power Sources 235 (2013) 74–80, https://doi.org/10.1016/j.jpowsour.2013.02.003
[75] Q. Fu, C. Tian, L. Hun, X. Wang, Z. Li, Z. Liu, et al., Ni agglomeration and performance degradation of solid oxide fuel cell: a model-based quantitative study and microstructure optimization, Energy 289 (2024) 129997, https://doi.org/10.1016/j.energy.2023.129997
[76] S. Yamatoko, M. Kishimoto, S. Buchaniec, Y. Guo, H. Iwai, Advanced 3D microstructure generation of solid oxide cell electrodes using conditional generative adversarial network and validation using nonintuitive topological characteristics, Adv. Intell. Discov. 1 (2) (2025), https://doi.org/10.1002/aidi.202500010
[77] Y. Huang, P. Zhu, S. Wang, X. Li, F. Yang, Z. Zhang, et al., Digital-electrode-based mesoscale analysis of degradation in solid oxide fuel cell anode, Cell Rep. Phys. Sci. 7 (1) (2026) 103035, https://doi.org/10.1016/j.xcrp.2025.103035
[78] Z. Wu, P. Zhu, Y. Huang, J. Yao, F. Yang, Z. Zhang, et al., A comprehensive review of modeling of solid oxide fuel cells: from large systems to fine electrodes, Chem. Rev. 125 (4) (2025) 2184–2268, https://doi.org/10.1021/acs.chemrev.4c00614